ELECTROCHEMICAL DETECTION OF CHEMICAL WARFARE AGENT SIMULANTS

A Thesis Submitted to the College of

Graduate Studies and Research

In Partial Fulfillment of the Requirements

For the Degree of Masters of Chemistry

In the Department of Chemistry

University of Saskatchewan

Saskatoon

By

ARMANDO J. MARENCO

PERMISSION TO USE

In presenting this thesis in partial fulfilment of the requirements for a Postgraduate degree from the University of Saskatchewan, I agree that the Libraries of this University may make it freely available for inspection. I further agree that permission for copying of this thesis in any manner, in whole or in part, for scholarly purposes may be granted by the professor or professors who supervised my thesis work or, in their absence, by the Head of the Department or the Dean of the College in which my thesis work was done. It is understood that any copying, publication, or use of this thesis or parts thereof for financial gain shall not be allowed without my written permission. It is also understood that due recognition shall be given to me and to the University of Saskatchewan in any scholarly use which may be made of any material in my thesis.

Requests for permission to copy or to make other use of material in this thesis in whole or part should be addressed to:

Head of the Department of Chemistry

University of Saskatchewan

Saskatoon, Saskatchewan

S7N 5C9

ABSTRACT

This work attempted to detect chemical warfare agent (CWA) simulants *via* electrochemistry utilizing two approaches. The first approach consisted of a ferrocene (Fc) amino acid derivative film on Au surfaces. The molecule $[(BocHN)Fc(CO)CSA]_2$ was electrodeposited onto Au microelectrodes through a S–Au bond. Once immobilized, the Fc amino acid derivative was Boc-deprotected allowing for the amino group to react with the target molecule. Detection of the target simulant was monitored by cyclic voltammetry (CV) while following the formal potential of the Fc molecule, which is influenced by its immediate electronic microenvironment. Reaction with either 1 mM diethyl cyanophosphonate (DECP) or 2-chloroethyl ethyl sulfide (2-CEES), both effectively simulants for the CWAs Tabun nerve agent and blistering sulfur mustard respectively, was not observed. However, detection of 1 mM acetyl chloride was achieved by observing a potential anodic shift from 217 ± 6 mV, for the Boc-deprotected form, to 388 ± 7 mV for the reacted state of the molecule. The lack of reactivity with the Fc amino acid system was hypothesized as a kinetic issue.

In the second approach, the electrochemistry of gas-generated naked Ag nanoparticles (NPs) deposited on indium-tin oxide covered glass plates is compared to bulk polycrystalline Ag. The nano-specific electrochemistry of Ag NPs has been identified and includes the preferential formation of β-oxides. In 100 mM KOH supporting electrolyte, disruption of β-oxide formation is exploited to test for the presence of 1 mM DECP resulting in the dissolution of Ag *via* cyanide complexes leading to a CV signal decrease. While in 8.0 M KOH, β-oxide formation is enhanced leading to testing capabilities for 1 mM 2-CEES resulting in the disappearance of the β-oxide peak and the appearance of surface oxide peak during CV. Analogous electrochemistry is not observed on polycrystalline bulk Ag.

ACKNOWLEDGMENTS

I would like to thank my supervisor Prof. Heinz-Bernhard Kraatz for his encouragement, help and support throughout this thesis.

I also would like to thank the following scientists at Defence R&D Canada – Suffield: Dr. David B. Pedersen and Dr. Shiliang Wang for collaborating with me and for their guidance; and Dr. Michael W. P. Petryk and Dr. William Lee for their moral and academic support.

I would also like to thank the members of my Advisory Committee Prof. Andrew Baranski, Prof. Marek Majewski and Prof. Dale E. Ward.

The acknowledgments could not be complete without thanking the members of the Kraatz group — the post-doctoral fellows Dr. Kagan Kerman, Dr. Piotr Diakowski and Dr. Xiaomin Bin; the graduate students Mohammad A. K. Khan, Yizhi Xiao, Grzegorz Orlowski, Mark Milne, Amir Kavianpour, Himadri Mandal, Khaled Mahmoud, Somenath Chowdhury, Haifeng Song, Anas Lataifeh, Samaneh Beheshti, Mervt Almostafa, Mohtashim H. Shamsi, Craig Colquhoun and Nina Hüsken; and the undergraduate students Demyan Prokopchuk, Marek Majewski Jr., Kirsten Tomlin, Cailin Drexler and Erin Morgan.

Finally, I would like to thank the Department of National Defence for the Civilian Personnel Education Support Program scholarship.

DEDICATION

To my parents.

TABLE OF CONTENTS

page

LIST OF TABLES

Table page

LIST OF FIGURES

Figure page

LIST OF ABBREVIATIONS

2-CEES	2-chloroethyl ethyl sulfide
ACh	acetylcholine
AFM	atomic forced microscopy
Boc	*tert*-butoxycarboxyl
CAM	Chemical Agent Monitor
CNT	carbon nanotube
CSA	cysteamine
CV	cyclic voltammetry
CWA	chemical warfare agent
DCM	dichloromethane
DECP	diethyl cyanophosphonate
EDX	energy-dispersive X-ray spectroscopy
E^o	formal potential
E_{pa}	anodic peak potential
E_{pc}	cathodic peak potential
Et_3N	triethylamine
Fc	ferrocene
GC	gas chromatography
HOPG	highly ordered pyrolytic graphite
IHP	Inner Helmholtz Plane
IMS	ion mobility spectroscopy
i_p	peak current
i_{pa}	anodic peak current
i_{pc}	cathodic peak current
ITO	indium tin oxide
JCAD	Joint Chemical Agent Detector
LC	liquid chromatography
LSV	linear sweep voltammetry
ME	microelectrode
MS	mass spectroscopy
NP	nanoparticle
O	oxidized species
OHP	Outer Helmholtz Plane
OPCW	Organization for the Prohibition of Chemical Weapons
R	reduced species
SAM	self-assembled monolayers
SAW	surface acoustic wave
SEM	scanning electron microscopy
STM	scanning tunnel microscopy
TFA	trifluoroacetic acid
UPD	underpotential deposition
WWI/II	World War I/II
Γ	surface coverage or footprint

CHAPTER 1
INTRODUCTION

Chemical warfare agents (CWAs) are toxic chemicals historically utilized in an effort to gain military superiority.[1] In recent modern history, they have been utilized on the battlefield as lachrymatory agents (causing respiratory irritation) during World War I (WWI) by the French and German armies. Due to the discovery of more potent agents, these non-lethal early chemicals are nowadays considered obsolete as warfare agents and thus used, for example, in riot control. The modern era of potent CWA utilization is considered to begin with the weaponization of chlorine and phosgene gases (causing lung damage) in 1915 by the German army.[2,3] Although these and other substances were banned for warfare use after WWI[4] by the 1925 Geneva Protocol, one of many treaties part of the Geneva Convention,[5] more potent CWAs such as sulfur mustard (causing epidermal blistering) were continually used by, for instance, the Italian army against Ethiopia in the 1936–1937 war and by the Empire of Japan against the Chinese during WWII.[2,3] Moreover, post-WWI and Nazi-ruled Germany continued CWA research and development in secret seeking to discover even more powerful and lethal agents,[6] while Allied nations starter their own research programs for protection and retaliation purposes.[3] It was in the mid-1930s that Nazi Germany discovered the highly toxic properties of organophosphorus nerve agents Tabun and Sarin with the addition of Soman in 1944.[6] In the 1950s, as part of pesticide research, an independent company in the United Kingdom discovered the most toxic of the standard nerve agents: VX.[2] This information was later shared with the United States of America. During the same period, with the help of spies, the former Soviet Union stole the molecular formula of VX, but without the chemical structure, Soviet scientists had to develop their own chemical version of the molecule which was later denoted Russian

VX.[7] These events are not without controversy as there are literature sources that indicate Soviet scientists developed this chemical compound on their own.[8]

In recent years, proliferation and weaponization of these chemicals has raised global alertness. During the First Gulf War (1981–1987) and after years of conventional warfare, Iraq turned to CWAs to fight against Iran and the Kurdish population of the area.[2,5] More recently, the Japanese religious cult Aum Shinrikyo utilized Sarin in two separate incidents in 1994 in Matsumoto city and in 1995 at the Tokyo underground transit system.[2,4,9] Thus, the recent misuse of CWAs on civilian populations and the threat of terrorist attacks on home soil has become a real scenario. Ideally, CWA detection using a cheap, fast and reliable method is desired.

1.1. Chemical Warfare Agents

1.1.1. Types of Chemical Warfare Agents

CWAs can be classified into seven categories based on their toxic effects on humans: nerve, blister or vesicant, chocking or pulmonary, vomiting, asphyxiant or blood, tear or lachrymatory and incapacitating agents (See Table 1.1).[1,3,10] Of these, nerve and blister agents present the most danger. The rest are currently considered obsolete agents as they are formulated to temporarily incapacitate target individuals rather than incur lethality.

Nerve agents are highly toxic organophosphates structurally related to insecticides. Nerve agents affect the body by irreversibly binding to organophosphorus acetylcholinesterase, a neurological enzyme which regulates acetylcholine (ACh).[10,11] ACh is a major neurotransmitter in the body that modulates the central nervous system directly affecting muscle activity. Once homeostasis is disrupted, ACh accumulation leads to a continual stimulation of the nervous system and eventual death.[1] Nerve agents are subdivided into the G- and V- series (see Fig. 1.1

AGENT TYPE	EFFECT	EXAMPLES
Nerve	Binds irreversible to acetylcholinesterase inhibiting acetylcholine (ACh) regulation. ACh accumulation leads to death.	G Series: Tabun, Sarin and Soman. V Series: VX
Blister or vesicant	Produces blistering of the skin. Also affects mucous membranes and eyes.	Sulfur mustard and nitrogen mustard.
Choking or pulmonary	Damages respiratory track and lungs.	Chlorine and phosgene.
Vomiting	Causes acute pain, nausea and vomiting.	Adamsite.
Asphyxiant or blood	Interferes with the adsorption of oxygen into the bloodstream.	Hydrogen cyanide.
Tear or lachrymatory	Induces tearing causing irritation to the eyes and skin.	Tear gas.
Incapacitating	Produces mental or physiological effects preventing normal activity.	Psychedelic agent BZ.

Table 1.1: Classification of the most common chemical warfare agents, their effects on humans and chemical examples. Adapted from ref. 2.

and Table 1.1). The main difference between the two series is the level of persistency once released onto the environment.[10] The term persistency refers to their resistance for hydrolysis and low volatility that characterize these chemicals. The V-series is the more persistent of the two.

Blister agents are responsible for blistering action acting on skin, but also can affect the eyes, mucus membranes and respiratory tract.[1,11] Compared to nerve agents, blister agents are weaker chemicals, as they require greater amounts to reach lethal doses.

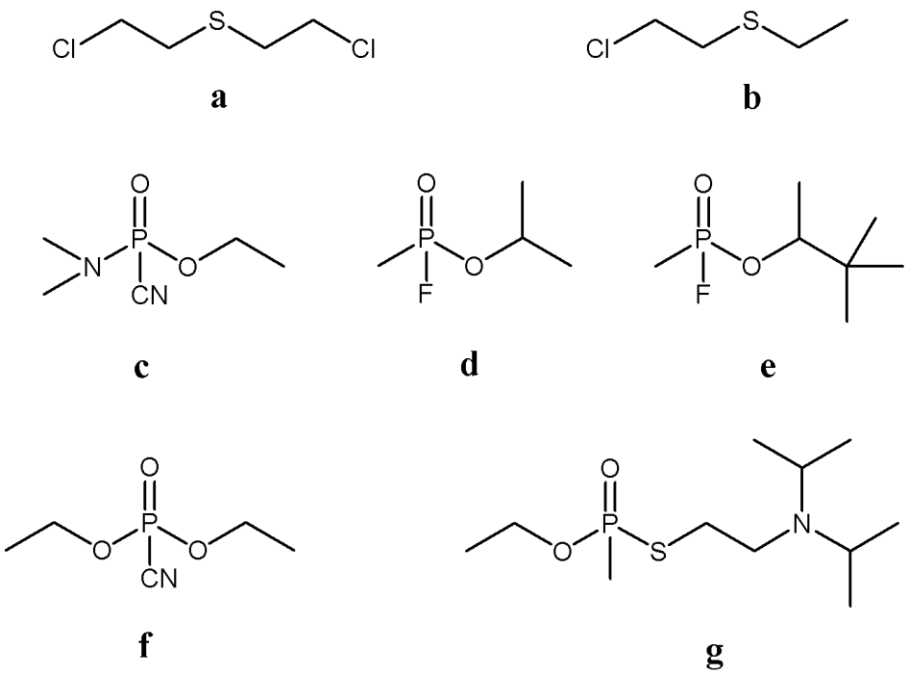

Figure 1.1: Chemical structures of the most common chemical warfare agents and effective simulants. The blister agent (a) sulfur mustard and its simulant (b) 2-chloroethyl ethyl sulfide. The nerve agents of the G-series (c) Tabun, (d) Sarin, (e) Soman and Tabun's simulant (f) diethyl cyanophosphonate. The nerve agent of the V-series (g) VX.

1.1.2. Physical Characteristics of Chemical Warfare Agents

Most CWAs exist as liquids at ambient temperature.[1,2] However, due to their various degrees of volatility (*i.e.*, persistency), these chemicals pose a hazard from different routes of exposure: percutaneous vapour (*e.g.*, vapour from contaminated terrain), vapour inhalation (*e.g.*, aerosols) and percutaneous liquid exposure (*e.g.*, direct contact).[1,12] Furthermore, hydrolysis products of some CWAs also show some level of toxicity and thus require detection for both protection and forensic analyses. For instance, water treated for drinking *via* distillation or reverse osmosis processes are very efficient in removing blistering CWAs hydrolytes; however, hydrolysis residues, such as thiodiglycol, are likely to infiltrate into the treated water.[13] Thus, assessing hydrolysis products or their intermediate chemical species is as important as the blistering agent itself.

1.1.3. Current Chemical Warfare Agent Detection, Identification and Monitoring Technologies

CWA samples can be found in two states: either in neat form (*i.e.*, as the final product of synthesis) or as contaminants on a matrix (*e.g.*, in soil samples or cloths items). In neat form, these samples would consist of relative pure chemicals and should contain little or no contaminants. Thus, they can be easily identified without the need for further purification methods using well-established laboratory techniques such as nuclear magnetic resonance. In many cases, when CWAs are present as contaminants, the first handling step is extraction followed by separation of the matrices before attempting to identify the types of chemicals present in the sample *via* a detector. Separation techniques such as liquid chromatography (LC),[14] gas chromatography (GC)[15] and capillary electrophoresis[16] have proven successful methods for CWA sample separation. These separation techniques are usually coupled to mass spectroscopy (MS) as a detection method.[14,17] Due to their physical properties, the method of choice for CWAs analytical handling is GC-MS;[2,18] moreover, it is the only approved technology for CWA identification by the Organization for the Prohibition of Chemical Weapons (OPCW). The OPCW is the implementing multinational body for the Chemical Weapons Convention which mandate includes the complete elimination of chemical weapons and to ensure their non-proliferation.[19]

Although GC-MS has some advantages over LC-MS, such as its simple mobile phase which avoids issues such as reagent imcompatibility, pH and solvent mix,[20] LC-MS is a good alternative for analysis of CWA aqueous samples. For example, separation of contaminated samples *via* this technique allows for the identification of CWAs and their hydrolysis derivates.[21,22] Unfortunately, these laboratory techniques require large pieces of equipment, controlled conditions and highly trained personnel to conduct such experiments. Some of these

drawbacks have kept these detection and identification methods inside laboratory settings and away from in-field applications. However, construction of mobile laboratories containing these pieces of equipment have allowed for some level of portability outside the laboratory and into required areas. Moreover, there have been recent attempts to bring these technologies out of the lab and onto the field in portable form.[23–25] Indeed, there has been an abundance of progress in the field of portable detectors based on MS but still there is a gap in these technologies required for field deployment.

Well-established in-field CWA detectors encompass several techniques and methodologies all attempting to satisfy a series of requirements based on the "ideal in-field detector". Among these requirements are portability, adequate sensitivity, ease of use, low maintenance and operation costs, reliability, selectivity, low susceptibility to interferences, ability for quantitative measurement and dynamic range[26] to mention a few. Unfortunately, none of the current in-field detectors satisfies all these requisites. For instance, most of these methodologies usually are semi-selective showing signs of cross-reactivity with interferences. Fortunately, portability is not an issue with these products. This permits an opportunity for a combinatory approach in which, for example, first responders and military force operations, employ several detector products in a single instance to improve characterization. Although accurate in-field characterization is ideal, in some of the circumstances presented to these individuals, the identification of a specific agent is not required as the personal protective equipment issued is interchangeable among CWAs. Their main concern is whether there is danger of exposure or not and whether there is the need for immediate precautionary measures.

For in-field detection the most common methods for CWA detection are briefly described below.

1.1.3.1. Colourimetric Methods

This technology was one of the first ones developed for CWA field analysis and is one of the simplest. Colourimetric-based detectors are made of pigment molecules impregnated into paper. When a specific target molecule in the liquid phase comes into contact with the colourimetric reagent, a chemical reaction occurs producing a colour change, which indicates the presence of the target chemical.[27,28] For instance, the commercial detection paper produced by Toyo Boseki contains two types of pigments together with a pH indicator impregnated onto cellulose paper.[29] When a G nerve agent comes into contact with the paper, the CWA is adsorbed and one of the pigments is solubilized producing a brown to orange colour change. On the other hand, if H blister agents are adsorbed the colour change is red as the other pigment gets solubilized. Finally, when a V nerve agent is adsorbed, the pH on the cellulose paper changes producing a black or deep green colouration. There are other similar products in the market such as the Paper Chemical Agent Detector produced by Anachemia Canada. In general, these products are simple (*e.g.*, no moving parts), ultraportable and easy to use.[27] Disadvantages include semiqualitative analysis by comparing intensity of colouration, moisture could affect its detection abilities, and it uses the human eye as a detector which varies widely in sensitivity.[27]

1.1.3.2. Ionization Methods

These detectors are based on the ion formation of vapour-phase samples followed by detection without separation. Due to their electric charge, ions can be "directed" by applying an electric or a magnetic field; thus, they are easy to manipulate and detect compared to neutral atoms or molecules.[30] There are two major ionization techniques found on such detectors: photoionization and flame ionization. In photoionization, a contaminated air sample passes

between two charged metal electrodes irradiated with high energy radiation such as ultraviolet light or X-rays,[27,28] while in flame ionization the air sample is burned in a high-temperature hydrogen flame.[27] In both techniques, the electric current generated can be correlated to the concentration of the species present.[27,28]

1.1.3.3. Surface Acoustic Wave Method

Detectors based on this technology study how acoustic waves travel on solid surfaces when these surfaces are under stress producing a signal change. In general, instruments possessing surface acoustic wave (SAW) technology consist of two transducers, one at each end of a solid surface.[31] The input transducer generates an acoustic wave in response to a time-varying electrical field, the acoustic wave then propagates along the solid surface, which is then transformed into an electrical signal by the output transducer.[32] The surfaces on which these waves travel require a piezoelectric material (*e.g.*, quartz). Piezoelectric materials allow for the transduction of an electric energy signal into a mechanical energy signal (*i.e.*, when a voltage is applied by the input transducer, the piezaoelectric material vibrates mechanically launching an acoustic wave towards the receiving transducer).[32] As with other wave-based studies, changes in amplitude or phase designate the detection abilities of the instrument. Thus, a typical chemical sensor is prepared when a piezoelectric material is coated with a film (usually consisting of a polymer) that adsorbs chemicals selectively onto its surface.[31]

An example of a detector utilizing the SAW technique is the hand-held Joint Chemical Agent Detector (JCAD). This detector consists of several polymer arrays capable of adsorbing several CWAs simultaneously. When the JCAD instrument is exposed to CWA vapours, they are

adsorbed selectively into the polymers which allow for SAW analysis.[29] In general, SAW-based detectors suffer from the difficult task of creating films that are chemically selective and stable.[31]

1.1.3.4. Flame Photometry

Detectors utilizing this methodology require the intake of an air sample believed to be contaminated with CWA vapour. The air sample is carried into the instrument and to a controlled hydrogen flame where the chemical components in the sample are burned. The controlled flame has a dual purpose: to incinerate the components in the sample and as colour quantification by the photosensitive detector.[28,29,33] When the contaminated air is ignited, the light emits wavelengths of different values as certain ion metals such as phosphorus and sulfur, which are two major components of most CWAs, will emit a characteristic wavelength when burned, allowing for detection of specific elements.[28,29,33] False positives are very common as there are several other non-CWA compounds containing either phosphorus or sulfur or both, especially in non-controlled scenarios.

1.1.3.5. Ion Mobility Spectroscopy

During ion mobility spectroscopy (IMS), an air sample containing vapour phase neutral molecules is drawn into the instrument where ionization, using photon- or radioactive ionization processes, takes place.[29,31] Ions in the gas-phase travel through a charged tube, where they are separated according to their size-to-charge ratio, before they collide with a detector plate.[28] At the detector plate, the plot of the current generated *versus* time produces a characteristic ion mobility spectrum, in which the peak current height is used to determine the concentration of agent present.[28]

The Chemical Agent Monitor (CAM) is the most commonly used IMS-based hand held detector in the field by the Canadian Forces. The CAM features two modes which allow selecting either blister or never agent detection but not both simultaneously. Unfortunately, it is susceptible to non-CWA false alarms triggered by, for instance, insect repellent and diesel fumes.

A disadvantage with all ion-forming technologies, including IMS, flame photometry and ionization methodologies, is that extremely low vapour pressure surface contaminants, such as the nerve agent VX, are not readily detected.[34] In addition, ions of similar mobility cannot be resolved, resulting in false alarms.[35]

Currently, there are no commercially-available electrochemical-based technologies in place for in-field detection of CWAs. However, there is an active research area in several electrochemical related fields including inmmunodetection,[36] carbon nanotubes (CNTs),[37] and nanoparticles (NPs).[38]

1.2. Electrochemistry as a Detection Method

Although electrochemistry has not yet established itself solidly in the CWA detection field, it has proven to be extremely successful in many other branches of industry (*e.g.*, food analysis), environmental and medical monitoring.[39] Electrochemical sensors for clinical analysis in non-hospital locations have seen the most success due to the expenses and time-consuming process usually accompanying the same studies in clinical laboratories.[40] These challenges have demanded clinical analysis at different locations, for example, at home by patients themselves. Electrochemical biosensors are ideally suited for non-hospital environments due to their high sensitivity, portable field-based size, rapid response time, simple to operate, and inexpensive operational capabilities.[40] These same characteristics are available for all electrochemical

detectors or sensor-based methodologies. Compared to mass spectrometric and chromatographic techniques (*i.e.*, GC-MS), electrochemical sensors are simpler in their setup and their electronic equipment requirements; are easier to maintain and calibrate; their signals are obtained directly *in situ*; and, are able to provide rapid response time. [40] However, the precision and detection limits that standard analytical methods provide cannot be yet matched by electrochemical sensors.[39] In general, the limitations of electrochemical sensors include electrochemically active interferences, long-term instability, and problematic electron-transfer pathways.[40] Nevertheless, current electrochemical sensors have proven that they complement the performance of conventional analytical tools by providing detection flexibility in non-clinical environments.

Electrochemistry as a sensor technology provides a wide variety of possible configurations due in part to the multitude of different techniques available, permutated with the different detection items available for such goal (*e.g.*, enzymes, CNTs and NPs). In general, an electrochemical sensor or detector functions by monitoring the properties of an electrical circuit when an analyte has interfere with the normal profile of the circuit.[28] Essentially, when target molecules enter the detection region, a chemical reaction occurs and produces a change in the monitoring electrical signal through an electrode.[28] In other words, electrochemistry implies the charge transfer from an electrode to another phase (*e.g.*, the molecule of interest or supporting electrolyte). In addition, the chemical reaction at the electrode and the process of charge transport can be modulated and serves as the basis of detection.[40]

1.2.1. Basic Electrochemical Principles

The electrochemical theory presented in this section is an attempt to briefly explain the concepts used in later chapters.

1.2.1.1. The Electrode-Electrolyte Interface

When an electrode is immersed into an electrolyte solution, it creates an interface region between the two components: the electrode surface and the adjacent layers of ions and solvent molecules from the electrolyte. This interface is known as the electrical double layer. At this phase boundary, a potential difference develops when, for example, a voltage from an external source is applied to the electrode creating excess electrons at the surface which are balanced by ions present in the electrolyte.[41] On the other hand, a potential difference can also be created by simply immersing the electrode into the electrolyte (*i.e.*, ions in immediate contact with the electrode surface will rearrange by anisotropic forces, in turn, forcing a charge rearrangement in the conductive material[42]). The two parallel layers of opposite and equal charge behave similarly to a capacitor-like structure.[41] A scheme of the double layer has been represented in Fig. 1.2.

The solution side of the double layer is made of several layers.[41] The layer closer to the electrode surface is known as the Inner Helmholtz Plane (IHP) and is made of solvent molecules and ions adsorbed onto the surface. The IHP is present exactly at the center of the ions adsorbed onto the surface. The layer containing the nearest fully solvated ions and separated from the electrode surface corresponds to the Outer Helmholtz Plane (OHP), and it is located at the centers of the solvated ions (*i.e.*, the ions and their solvent shells). The solvated ions interact with the electrode surface only by electrostatic forces.[41] Beyond the OHP, the diffuse layer is found. The diffuse layer contains the rest of the solvated ions, solvent molecules and extends to the bulk solution. The double layer capacitance is the result of both the capacitance of the compact layer (*i.e.*, the Helmholtz planes) and of the diffuse layer similar to a capacitor-in-series system, as such, the double layer capacitance decreases as the double layer thickens.[43]

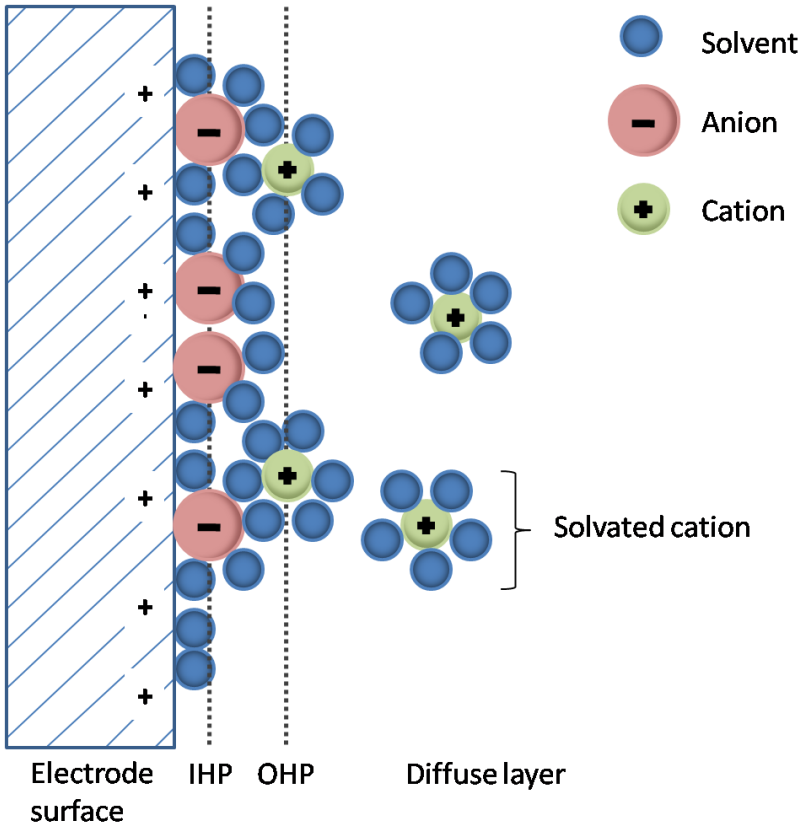

Figure 1.2: Diagram of the electrode-electrolyte interface. The center of the anions adsorbed onto the electrode surface form the inner Helmholtz plane (IHP). The center of solvated cations nearest to the electrode surface form the outer Helmholtz plane (OHP). Solvated cations, solvated anions and solvent molecules form the diffuse layer. Adapted from ref. 41.

The double layer is where the electrochemistry happens.[41] When the equilibrium of this capacitor is broken, the process of charge transfer follows. When the applied potential in the electrode is driven highly positive electrons are transferred from the solution to the electrode surface. This is the oxidation process. On the other hand, if the applied potential is highly negative, electrons are transfered from the electrode to the ionic solution in the process called reduction. In cases where there is a redox species bound to the surface of the electrode, the electron transfer occurs through this species.[44]

1.2.1.2. Factors Affecting Electrode Reaction Rate

In general, an electrode reaction involving a redox species in solution can be written as $O + ne^- \rightleftharpoons R$, where O refers to the oxidized species that is converted into the reduced form R by the addition of *n* number of e^- electrons.[41] The electrode reaction rate (*i.e.*, the current) is affected, in the simplest of cases, by two main factors: mass transfer and electron transfer at the electrode surface (see Fig. 1.3).

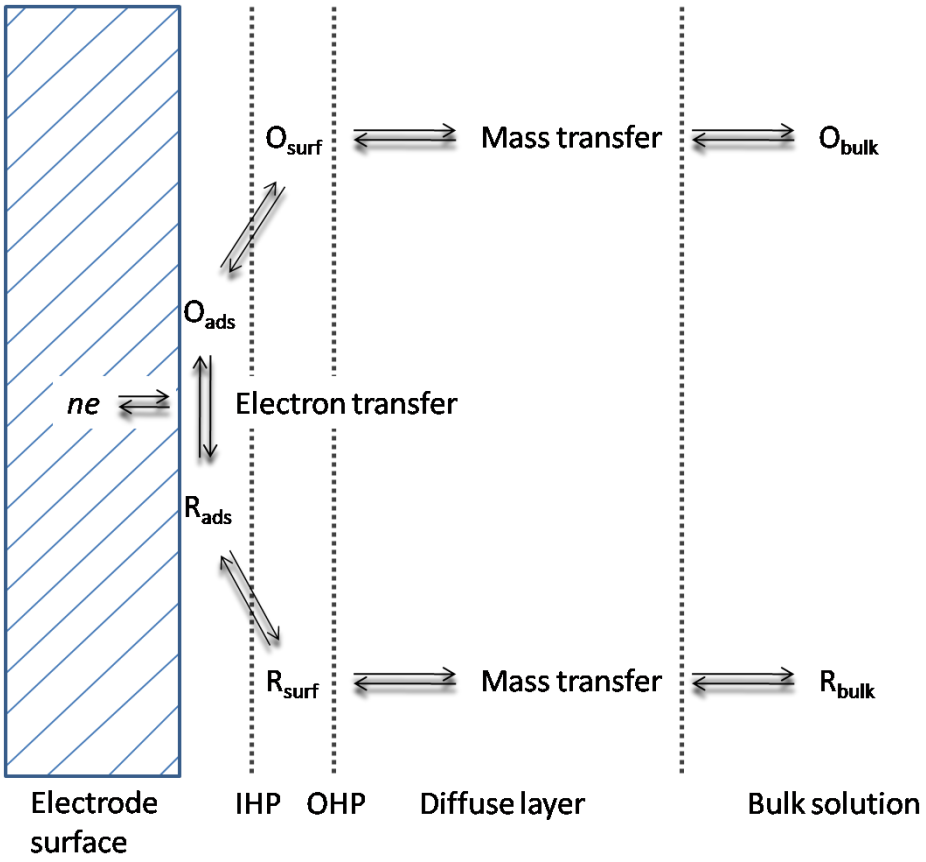

Figure 1.3: Diagram of the process of mass transport and electron transfer at the working electrode surface. Species O_{bulk} diffuses through the different layers until it reaches the electrode surface (O_{surf}). At the surface, the species is adsorbed (O_{ads}) and is reduced to form R_{ads}. R_{ads} desorbs from the surface and diffuses away towards the bulk solution (R_{bulk}). Adapted from ref. 41.

Mass transfer refers to the process by which species O travels from the bulk of the solution towards the electrode surface.[41] In Fig. 1.3, species O travels from the bulk, through the diffuse layer, the OHP and the IHP to be at the electrode surface. At the surface, species O is adsorbed by the electrode before the process of electron transfer takes place. At this stage, species O is reduced to R. Species R is then desorbed from the electrode and its journey is opposite that of O. As such, the movement of species R away from the electrode surface is also mass transfer. Thus, the reduction or oxidation of a substance at the working electrode surface, driven by the applied potential, generates redox current (*i.e.*, Faradaic current).[41] Finally, this current is limited by the diffusion of ions to and from the electrode as will be explained in section 1.2.2.1.

In cases where the electrode has been modified by binding the redox molecule onto the electrode surface (*i.e.*, no redox species present in solution), the current is no longer controlled by diffusion. In surface electrochemistry cases, the process of electron transfer plays a more important role.

1.2.1.3. The Electrochemical Cell

The electrochemical cell is the physical boundary in which experiments are performed. This cell contains two main components: the supporting electrolyte and several electrodes. The supporting electrolyte is the conductive medium which facilitates charge transport. The nature (*e.g.*, organic *vs.* inorganic) and physical phase (*e.g.*, liquid *vs.* gel) of this component is immensely flexible adapting it to meet the needs of the research. When describing electrodes, there are at least two required to perform an electrochemical experiment. So far, when the word electrode has been mentioned, it has been referring to the working electrode. The working electrode is the location for the redox reaction and where the current monitoring (*i.e.*, the

experimental variable) takes place. A second electrode in the system is the reference electrode. The reference electrode serves as a measure of the magnitude of the voltage applied to the system. In other words, the external potential (*i.e.*, voltage difference) applied to the working electrode is controlled by comparing its value to the reference electrode fixed potential. For this reason, the reference electrode is characteristically non-polarisable with changing voltage (*i.e.*, its potential remains stable during a small passage of current). However, in a two-electrode setup, current is forced to pass through the reference electrode whenever a measurement is made and if enough current flows through it, the potential could drift from its standard value.[45] This is easily avoided in a three-electrode system in which an additional electrode, the counter or auxiliary electrode is utilized. In summary, the potential applied into the electrochemical system by the potentiostat to the working electrode is controlled *via* the reference electrode and the current flowing between the working electrode and the counter electrode is measured and reported.

1.2.2. Electrochemical Techniques Applied in this Research

The electrochemical techniques utilized in this research are exclusively voltammetric in nature. Voltammetry refers to those techniques where the applied potential is the controlled variable while the current flowing through the electrochemical cell is the measured variable.[45,46]

1.2.2.1. Linear Sweep Voltammetry

In a linear sweep voltammetry (LSV) experiment, a potential range is applied to the working electrode at a constant rate starting from a lower limit voltage (V_0) to an upper limit value (V_1) (see Fig. 1.4a). The applied potential range must contain the formal potential of the analyte

under investigation.[45] A voltammogram is obtained when the resulting measured current is plotted against the applied potential (see Fig. 1.4b). By incorporating the formal potential value of the analyte within the applied potential range, the current response is at first low (*i.e.*, at and near the voltage lower limit). As the voltage is ramped further to the upper limit, the current begins to flow eventually peaking before dropping.[45]

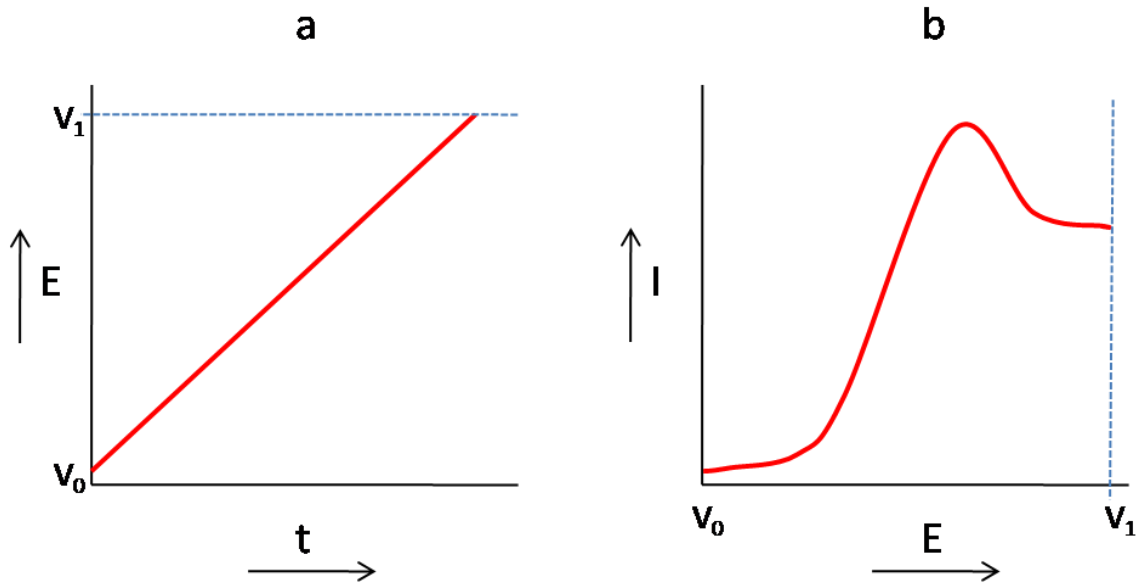

Figure 1.4: Graphical representation of LSV. (a) The potential window applied in a LSV experiment from the lower voltage limit V_0 to the upper voltage limit V_1. (b) Current response in a simulated LSV experiment. Adapted from ref. 41.

The current response can be explained in terms of analyte concentrations near the working electrode surface as described in section 1.2.1.2. At voltages near V_0, there is no enough potential energy to reduce O to species R (assuming only species O is present at the start of the experiment). The current at this stage is small as there is a small flow necessary to maintain the double layer charged at the electrode, thus called the charging current.[47] As the potential energy required to reduce O to R is reached, the O molecules adsorbed at the electrode surface are reduced to R species. R molecules are transported towards the bulk solution away from the

electrode surface allowing O molecules to be transported from the bulk solution towards the electrode surface. This mass transport process permits the electron transfer phenomenon to occur and thus the increase in the Faradaic current. Current peaks and starts decreasing once O molecules need to travel from greater distances to reach the electrode surface. The measured Faradaic current becomes a function of the diffusion of species O to the electrode as it is limited by the mass transport process.[47]

1.2.2.2. Cyclic Voltammetry

Cyclic voltammetry (CV) is probably the most popular electrochemical technique utilized by researchers.[48] This is because it is relatively easy to gather and contains a multitude of information. CV is very similar to LSV. In a CV experiment, an initial potential (V_0) is applied to the working electrode at a constant rate (Fig. 1.5a). The voltage is sweep to an upper limit (V_1) before it is reversed to a lower limit (V_2). Then, the voltage is scanned from V_2 back to V_1. This ensuing cycling between voltage values results in the name of the technique.

In this technique, the information is presented by plotting the current against the potential range resulting in a cyclic voltammogram graph (Fig. 1.5b). It is common practice, although not technically correct, to refer to both, the technique and the resulting plot, as CV.

The information obtained from a CV graph consists of the anodic peak current (i_{pa}), the cathodic peak current (i_{pc}), the anodic peak potential (E_{pa}) and the cathodic peak potential (E_{pc}). E^o is the formal potential for the reversible redox couple and is calculated as follows:

$$E^o = (E_{pa} + E_{pc}) / 2 \qquad \text{(Equation 1)}$$

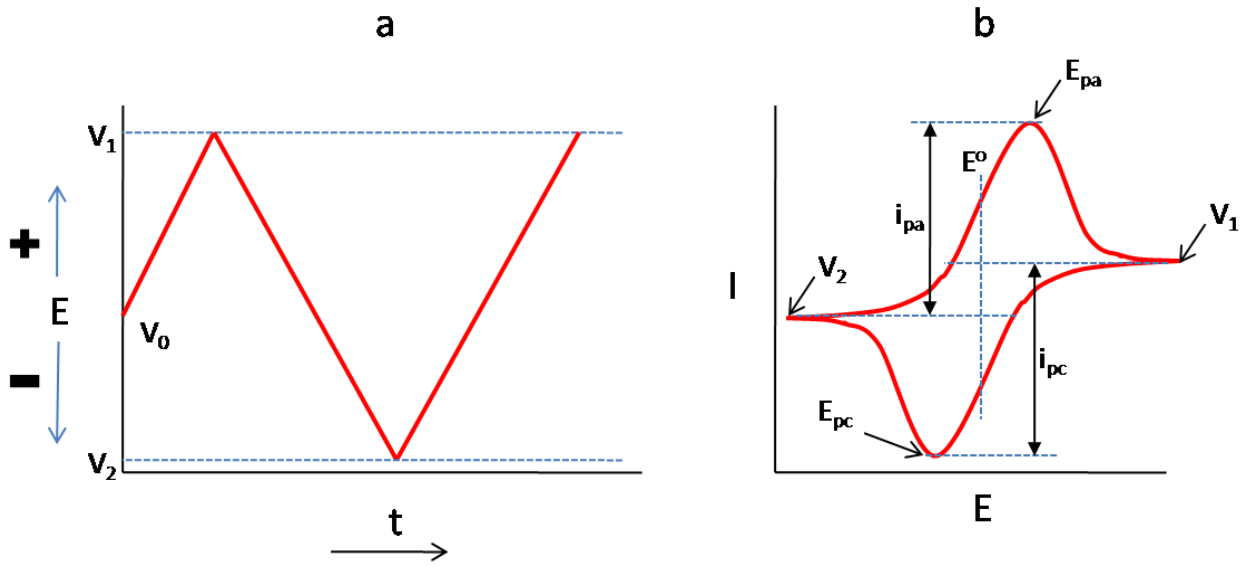

Figure 1.5: Graphical representation of CV. (a) The potential range applied in a CV experiment starts at the initial voltage limit V_0, it ramps to the upper voltage limit V_1, and then it is reversed to a lower voltage limit V_2, before it returns back to V_1. The potential sweep from V_1 toV_2 and back to V_1 is a cycle. (b) Current response in a simulated solution CV experiment. Adapted from ref. 41.

For this reason, E^o is also known as half-wave potential and also designated as $E_{1/2}$. The *measured* E^o is part of the Nernst equation:

$$E = E^o + R\,T / n\,F\,(\ln C_O/C_R) \qquad \text{(Equation 2)}$$

where E is the potential applied to the cell, R is the universal gas constant (8.314 J/mol K), T is the absolute temperature (K), F is Faraday's constant (96485 C/mol), n is the number of electrons in the redox process, and C_O and C_R are the concentrations of species O and R respectively. Thus, the Nernst equation is able to link the electrode potential E and the concentration of the analyte in the redox process. It is worth noting that this equation is a modified form of the Nernst equation as it contains concentration values rather than activity factors (*i.e.*, C_O/C_R instead of a_O/a_R). Activities are unitless factors containing activity

coefficients most of which are almost always unknown,[41] rendering activity values inconvenient to work with compared to concentrations. Therefore, the E^o formal potential factor incorporates the activity coefficients.[41]

The magnitude of the reduction or oxidation current in a CV experiment is proportional to the concentration of the analyte, which allows this technique to be used as an effective electroanalytical tool.[45] The peak current, for either i_{pa} or i_{pc}, in a reversible diffusion limited system is described by the Randles-Ŝevi$\hat{c}$k equation:[49]

$$i_p = 0.4463\ n\ F\ A\ C\ (n\ F\ \upsilon\ D\ /\ R\ T)^{1/2} \qquad \text{(Equation 3)}$$

where A is the electrode area (cm^2), υ is the scan rate (V/s) and D the diffusion coefficient (cm^2/s) of the analyte. Factors n, F, C, R and T have already been described for Equation 2. Equation 3 can be simplified by assuming a temperature value of 25^{o}C, equivalent to 298.15 K, and is also found in the literature as follows:[50]

$$i_p = (2.687 \times 10^5)\ n^{3/2}\ A\ C\ \upsilon^{1/2}\ D^{1/2} \qquad \text{(Equation 4)}$$

where the constant is assumed to have units of $C\ mol^{-1}\ \upsilon^{-1/2}$.

Until now, the scenario described has been for a solution system in which the analyte (in both oxidized and reduced forms) is present freely in the electrolyte thus unbound to the electrode surface. In other words, it describes a reversible solution system controlled by the process of diffusion. Another possible case scenario is when the analyte is bound to the electrode surface. In this case, it is assumed that only species O is present at that O is not dissolved in the electrolyte. In a system with such characteristics, diffusion does not play a role. For this reason, the CV graph for a species absorbed onto the electrode differs from that of a solubilized redox compound (*cf.* Fig.1.5b and 1.6).

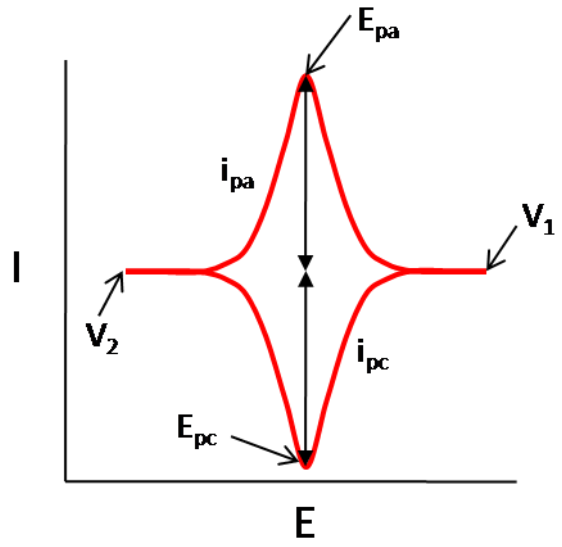

Figure 1.6: Graphical representation of the current response in a simulated CV experiment in which the analyte is adsorbed onto the electrode surface. Adapted from ref. 41.

Furthermore, since mass transfer is eliminated as a factor, the current is affected during the redox process as shown in the following equation:[41]

$$i_p = (n^2 F^2 / 4 R T) A \Gamma \upsilon \qquad \text{(Equation 5)}$$

where Γ is the surface coverage or footprint of the molecule bound onto the electrode surface. This variable can be calculated using the following equation:

$$\Gamma = Q / n F A \qquad \text{(Equation 6)}$$

where Q is the charge of the integrated cathodic or anodic peak.

A key similarity between solution and surface electrochemistry reactions is that for a reversible redox compound, the current ration i_{pa}/i_{pc} is equal to 1. Conversely, a key difference between them is the current relationship to the applied scan rate: for a solution reaction, i_p is directly proportional to $\upsilon^{1/2}$ (see Equation 3 and 4), while for a surface reaction, i_p is directly proportional to υ (see Equation 5).

1.3. Objective

Electrochemistry, as a detection technique, has the capability for miniaturization without loss in analytical performance,[37] making it amenable to a lab-on-a-chip approach. Miniaturization, consecutively, adds to the potential advantage of electrochemical detection as the requirements for consumables and power could be significantly reduced over other methodologies. Research on electrochemical detectors for nucleic acids, immunodetectors and gases utilizing CNTs, NPs and ferrocene (Fc)-based compounds can be found readily available in scientific literature.

The major objective of this thesis research was to determine if it is possible to detect CWA simulants electrochemically. Two systems were tested in order to reach this objective: the chemical modification of Fc amino acid derivative and the interaction of CWA simulants with silver NPs. In the first approach, described in Chapter 2, reaction of the amino group is exploited and the redox potential of the Fc-containing molecule is monitored as a function of added CWA simulant. The Fc amino acid molecule is chemically attached as a film to the working gold microelectrode. The redox potential of this molecule is altered when CWA simulants bind selectively to the amino group and is detected by CV measurements. In the second approach, NPs present physical properties not observed in their bulk analogues. A conductive substrate is modified with silver NPs and then exposed to CWA simulants. The presence of simulants affects the electrochemical characteristics of NPs. Chapter 3 will discuss the results of these studies in detail and provide an in-depth discussion of the changes that occur as a function of CWA simulant addition.

Finally, Chapter 4 will provide a summary of the research accomplishments, discuss them in the context of existing technologies, and provide a brief outlook of future research.

CHAPTER 2
FERROCENE AMINO ACID DERIVATIVE SYSTEM

Ferrocene (Fc) is a neutral molecule containing two cyclopentadienyl rings sandwiching a Fe(II) centre. Since its discovery in 1951,[51] Fc has become a very versatile molecule. In the medical field, due to its non-toxicity and chemical stability properties, ferrocenyl compounds (*i.e.*, Fc containing compounds) have been researched to combat diseases such as malaria and several forms of cancer.[52] In the field of electrochemistry, Fc exploitation is based on its excellent redox and stability qualities. This neutral organometallic molecule is able to loose an electron to form the stable ferrocenium cation during its oxidation process (Fig. 2.1). Examples of Fc derivatives utilization in electrochemical detectors for DNA,[53] proteins[54,55] and CWAs simulants[37,56] sensors are available in the literature. The appeal to work with Fc in electrochemistry is that it can be easily modified with different reacting groups allowing to adjust the chemistry to that of the analyte under study.

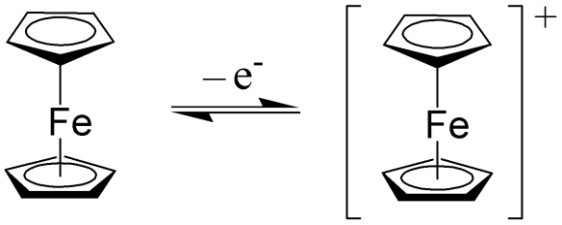

Figure 2.1: Ferrocene redox reaction in which the molecule looses an electron to become the stable ferrocenium cation.

2.1. The Ferrocene Amino Acid Derivative System

This electrochemical detector system consisted of the Fc amino acid derivative $[(BocHN)Fc(CO)CSA]_2$ molecule (Fig. 2.2a) covalently bound to Au (Fig. 2.2b). This molecule contains three major components. It contains (i) a cystamine linker that allows for surface

assembly through a S–Au bond. The molecule dissociates into two equivalent halves at the disulfide bond once immobilized onto the surface, transforming the cystamine into two cysteamine (CSA) molecules. In this form, each half molecule contains (ii) a Fc molecule as the redox probe and (iii) a terminal functional amino group as the reacting site for CWAs and their simulants. The amino group is unable to chemically react due to the *tert*-butoxycarboxyl (Boc) protecting group bound to it. Once the Boc protecting group has been chemically removed at the convenience of the user, the amino group is able to react with the analyte. The analyte bound to Fc will ultimately influence its redox potential due to the ability of the analyte to either withdraw electrons (*i.e.*, the resulting molecule becomes harder to oxidize thus observing an anodic shift on a CV scan) or donate electrons (*i.e.*, easily to oxidize thus observing a cathodic shift on a CV scan). In other words, the Fc potential is influenced by its immediate electronic microenvironment.[57,58] Electrochemical monitoring of the three different Fc amino acid derivative stages (namely Boc protected, Boc deprotected and reacted molecule) should allow for the analysis of CWAs and their simulants.

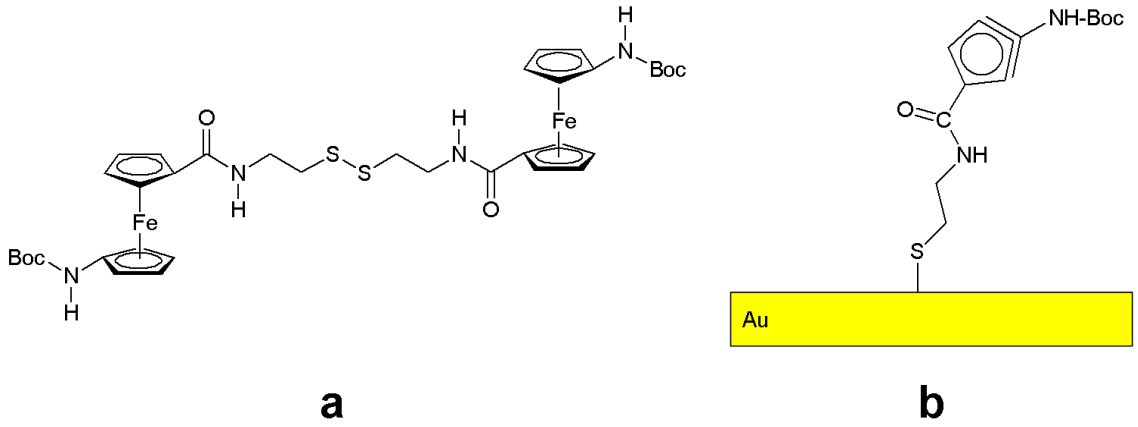

Figure 2.2: Molecular structure of $[(BocHN)Fc(CO)CSA]_2$ (a) unbound and (b) bound to a gold surface *via* a dissociated disulfide bond. Adapted from ref. 56.

2.2. Films of $[(BocHN)Fc(CO)CSA]_2$ on Gold Surfaces

2.2.1. Self-assembled Monolayers

The initial films created with the Fc amino acid derivative were obtained by self-assembling of molecules from solution. The phenomenon of self-assembled monolayers (SAMs) of thiols onto Au, especially of alkanethiols (*i.e.*, RS–H), has been extensively studied.[59] SAMs, in general, describe a spontaneous organization and chemical binding of molecules in either solution or gas phases into dense crystalline structures onto a substrate.[60] In the case of the RS–Au SAMs, the process is driven by the high affinity of thiol sulfur to the Au metal surface due to the energetically favoured strong bonding between them (*ca.* 50 kcal/mol[61,62]). This affinity also helps at displacing adsorbed species bound to the Au surface by the sulfide-containing molecules.[61] Another aspect that helps the formation and crystalline characteristics of SAMs is the intermolecular interaction of the alkyl chain. The neighboring alkyl chain molecules interact laterally through van der Waals forces to add stabilization to the film.[63,64] On the other hand, those alkanethiols molecules containing a terminal group (*i.e.*, other than a methyl from the alkyl chain), could add instability to the film if chosen unwisely. The terminal group confers properties to the layer (*e.g.*, hydrophobicity or hydrophilicity) and small changes affect its physical and chemical properties.[65] More importantly, the relative size of this group, compared to its anchoring alkyl chain, can complicate self-organization and compactness due to steric effects.[61,66]

Although thiols have been used extensively for SAM purposes, other sulfur containing compounds have been studied, for instance dialkyl disulfides (*i.e.*, RS–SR) and dialkyl sulfides (*i.e.*, RSR).[67,68] An observation with the use of dialkyl disulfides is that films could result in multilayer formation (rather than a one-layered film as in SAMs) by precipitation due to their lower solubility compared to thiols.[65]

It is generally agreed that SAM preparation from solutions is an easy process, which requires simply immersion of the Au surface (*e.g.*, electrode) into the sulfide-containing solution.[65] However, it is also agreed by workers in the field that their preparation is a dynamic process[62] and the optimistic views of a perfect SAM (*i.e.*, a full surface coverage film free of imperfections) is not achieved easily,[66,69] in turn leading to irreproducible data.[70] Thus, continuing researchers in this field are successful at their craft.

Some of the factors affecting the quality of SAMs include:

- Incubation time: Au surfaces exposed to alkanethiols solutions are coated with a film within seconds of exposure.[69] However, these films are not well organized (*i.e.*, contain defects) and do not provide a full surface coverage. To achieve dense and crystalline films, substrates require hours or even days of exposure. The most common defect found in SAMs is pinholes consisting of vacant islands exposing the substrate among a sea of monolayer. Using permeability studies with solution redox couples have shown that even after extensive incubation, pinholes populate the surface at $\leq 1\%$.[71]

- Substrate: Since the ligand group binds the substrate, any heterogeneities or contaminants bound to the surface will define the formation quality of the film. As a result, the polycrystalline characteristics of the substrate play a critical role in preparing SAMs. For instance, when using electrodes for SAMs, a contaminant-free surface is achieved by physical polishing the exposed surface area, by repeated electrochemical cycling, or a combination of both.

- Clean sulfide solution free of contaminants: Contaminant species present in the sulfide-containing solution could co-adsorb onto the surface. This may lead to thin films and unwanted electrochemical interactions in the case of a redox active contaminant.

- The terminal group: As discussed above, the terminal group must be of acceptable size to avoid collapsing of the molecule at the surface. Collapsing or physisorption of the molecule at the surface could give rise to a disorganized film or the creation of pinholes.
- Length of alkyl chain: This part of the molecule acts as a spacer between the metal surface and the end group, thus defining the SAM thickness. The length of the chain will affect, among other aspects, the crystallinity of the film via lateral van der Waals interactions[63,64] and the electron transfer rates (*e.g.*, distance dependency) which is achieved through the chain.[44,72]

2.2.1. Electrodeposition Method

As discussed in the previous section, the list of factors affecting the quality of passive deposition of SAMs is quite lengthy. Moreover, the reproducibility of such films under passive-solution deposition is usually difficult even though identical preparation conditions were applied. Potential-assisted deposition (*i.e.*, electrodeposition) is able to improve in two important factors over passive deposition: reproducibility with high-quality extensive surface-blocking films and preparation time reduction from days to minutes.[70]

Passive-solution and potential-assisted deposition methods are based on the fact that during adsorption, thiols are deprotonated as follows: $RS–H + Au \rightleftharpoons RS–Au + e^- + H^+$.[73] By providing a reducing potential, it is argued that the thiols are deprotonated/reduced quicker creating faster films. Nevertheless, the observations described by several research groups are that electrodeposition creates faster and more compact films compared to passive solution deposition.[70,74] The denser films created via electrodeposition can be explained by understanding that during passive incubation deposition, the surface reaches a potential at which chemisorption is not further energetically favourable.[70] It is important to note that our working

molecule is a disulfide and not a thiol; regardless, a large negative potential would reduce disulfides to thiolate anions facilitating film assembly.[74]

2.3. Results and Discussion

During SAM films of $[(BocHN)Fc(CO)CSA]_2$, several electrochemically treated Au microelectrodes (MEs) were incubated at once. After the 5-day incubation period in a 1 mM ethanolic Fc amino acid derivative solution, the treatment required sonication in ethanol and incubation in a 1 mM ethanolic solution of butanethiol. The sonication allowed for the removal of physisorbed or weakly adsorbed molecules onto the Au surface. The butanethiol solution allowed for backfilling of exposed Au surface created during the sonication process or due to pinholes and other defects. In general, films resulting from this method were much diluted and those MEs with good coverage were scarce (approximately 10% of MEs per experiment were considered good coverage). Of these, when Boc deprotection and/or CWA stimulant exposure was attempted, the Fc signal would disappear most likely due to desorption of molecules by the deprotection process.[56] Although these signal-absent MEs were not further analysed, for instance with ferri/ferrocyanide solutions to study surface coverage post-deprotection, some studies suggest the possibility of film disorder as the cause of considerable reduced signal.[67]

For a typical SAM film, the footprint (*i.e.*, Γ, the real state area in $Å^2$ occupied per molecule bound onto the surface) was 150 in average. This result is in contrast to the ideal value of 36, but within previous experimental Γ values of 130 ± 51 by the passive deposition method.[56] The inconsistency and low success rate achieved with the SAM method led to seek a more reliable method for film formation.

Electrodeposited films of $[(BocHN)Fc(CO)CSA]_2$ were consistently stable after electrochemical cycling in electrolyte. It is worth noting that in this method, both sonication and

backfilling procedures were also applied. Unlike passive solution deposited films, cycling of *Boc-protected* films were very stable and decreasing signal intensity was hardly an issue even after several cycles (Fig. 2.3).

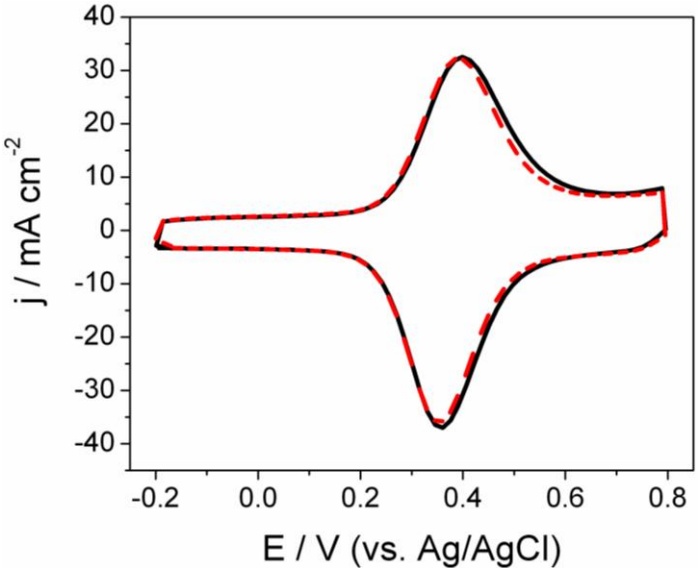

Figure 2.3: CV scans of $[(BocHN)Fc(CO)CSA]_2$ films electrodeposited onto 50 μm gold microelectrodes. Stability of the film was tested by cycling 50 times (red dashed trace) compared to the first cycle (black solid trace). CV scans recorded at 100 mV/s scan rate in 2.0 M $NaClO_4$ *vs.* Ag/AgCl utilizing a Pt wire as the counter electrode.

In order to further characterize electrodeposited films of the Fc amino acid derivative, several scan rates were applied to a typical film. Plotting the peak current density against the scan rate for a film of $[(BocHN)Fc(CO)CSA]_2$ on gold, shows a linear relationship (Fig. 2.4b). A linear relationship is expected for a surface-bound species indicating the successful immobilization of the compound onto gold surfaces. See Equation 5 in section 1.2.2.2.

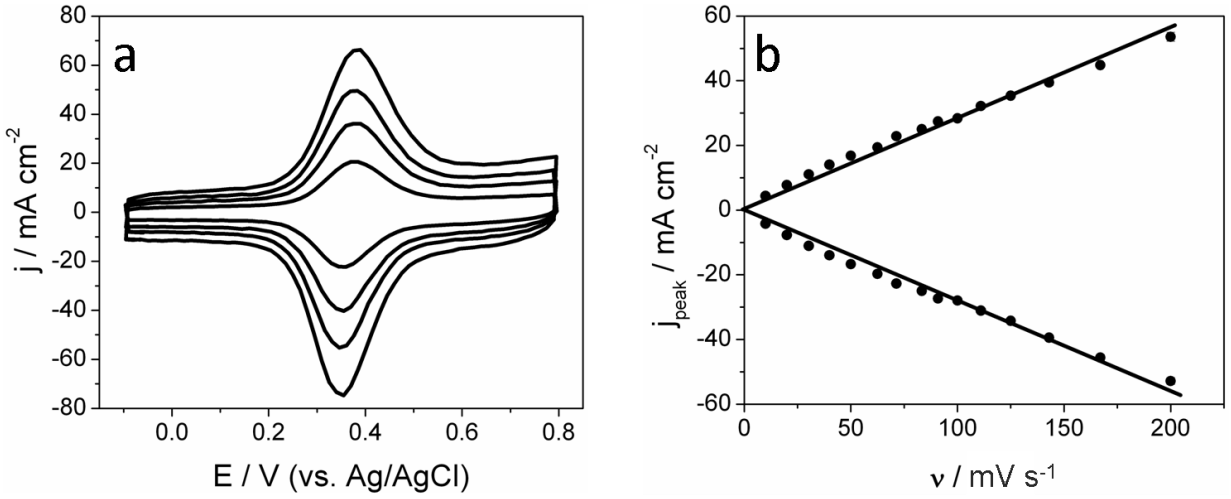

Figure 2.4: (a) CV scans obtained at 50, 100, 143 and 200 mV/s scan rates for an electrodeposited film of $[(BocHN)Fc(CO)CSA]_2$ onto gold; (b) plot of peak current density *vs.* scan rate for the film in plot (a). CV scans recorded in 2.0 M $NaClO_4$ *vs.* Ag/AgCl utilizing a Pt wire as the counter electrode.

A comparison of CV scans obtained for $[(BocHN)Fc(CO)CSA]_2$ films onto gold by passive solution deposition and by electrodeposition is shown in Fig. 2.5 (a and b, respectively). Although this figure shows CV scans of very similar high density (*i.e.*, Γ in unassisted deposition is 78 (± 11) $Å^2$ *vs.* 48 (± 6) $Å^2$ in potential assisted deposition), the consistency in film density found in the electrodeposited films was far superior.

The formal potential (E^o) values determined by both methods are virtually within the experimental error calculated (Fig. 2.5). However, these values are distant from similar reported studies in which a E^o of 317 (±15) mV for solution deposition films was determined.[56] This difference points to film variations under the same conditions, and it also points to the differences incorporated by the individual researcher. Hence, determining the value of E^o for each film in the Boc-protected state is required in this study. Also from Fig. 2.5, the current ratios determined by both methods are 1, or close to unity, suggesting a reversible redox reaction.

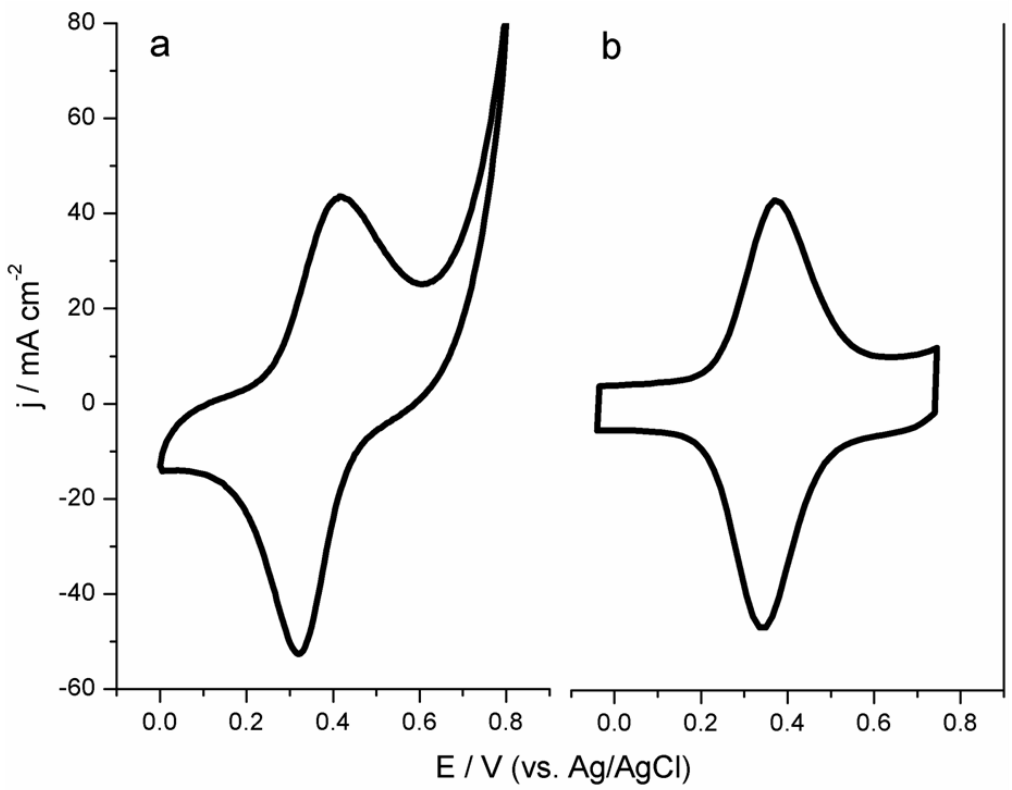

Method	Γ (Å²)	E° (mV)	ΔE_p (mV)	i_{pa} / i_{pc}
a	78 (±11)	368 (±5)	95 (±8)	0.90
b	48 (±6)	356 (±6)	28 (±4)	1.01

Figure 2.5: CV scans comparison of $[(BocHN)Fc(CO)CSA]_2$ films deposited onto 50 μm gold microelectrodes by (a) conventional SAM solution deposition and (b) electrodeposition. The accompanying table describes the footprint or surface coverage (Γ), the formal potential (E^o), the peak position difference (ΔE_p) and the current ratio (i_{pa}/i_{pc}). Errors are the standard deviations from five measurements. CV scans recorded at 100 mV/s scan rate in 2.0 M $NaClO_4$ vs. Ag/AgCl utilizing a Pt wire as the counter electrode.

It is worth noting that the shapes of the CV scans of the same molecule by the two methods shown in Fig. 2.5 are different. This is exemplified by the peak potential difference (ΔE_p) values. Due to the lack of diffusion processes, the ideal ΔE_p for a redox molecule bound to the surface is equal to 0 (see Fig. 1.6 in Ch. 1). Solution unassisted deposition (Fig. 2.5a) shows a

ΔE_p of 95 (±8) mV. This result is not unusual as values distant from the ideal figure have been observed by others in surface-bound electrochemical experiments.[56,67] Electrodeposition (Fig. 2.5b), on the other hand, shows a value of 28 (±4) mV.

The effects described on this section and their difference from ideal values is most likely the results of film disorganization as redox molecules face different microenvironments within the film. This could further indicate the inherent heterogeneity nature of the films as each particular film shows individuality.

2.3.1. Boc Deprotection and Chemical Warfare Simulant Detection

Deprotection of the Boc group from $[(BocHN)Fc(CO)CSA]_2$ films on gold turned out to be a harsh process for the film. The standard procedure for Boc removal from amino acids is with a 50% solution of trifluoroacetic acid (TFA) in dichloromethane (DCM).[75] Previously reported studies with $[(BocHN)Fc(CO)CSA]_2$ films onto gold utilized a similar procedure employing a 40% TFA in DCM solution for 1 min.[56] After Boc removal, the amino group immediately attached to Boc required deprotonation for the *reacting form* of the system to occur. This latter Boc deprotection procedure,[56] continued with washing the unprotected film using ethanol followed by water, then exposing the modified ME to a 10% ammonium hydroxide (NH_4OH) in water for 15 sec for the deprotonation step, and finally exposing it to CWA simulant dilutions. After numerous failed attempts to perform this particular procedure and variations of it, our modified procedure consisted of: 1 min in 10% TFA in DCM, followed by 10 sec in a solution of 10% triethylamine (Et_3N) in DCM and exposure for 1 min CWA simulant solutions. The process of Boc deprotection and chemical exposure is presented in Fig. 2.6.

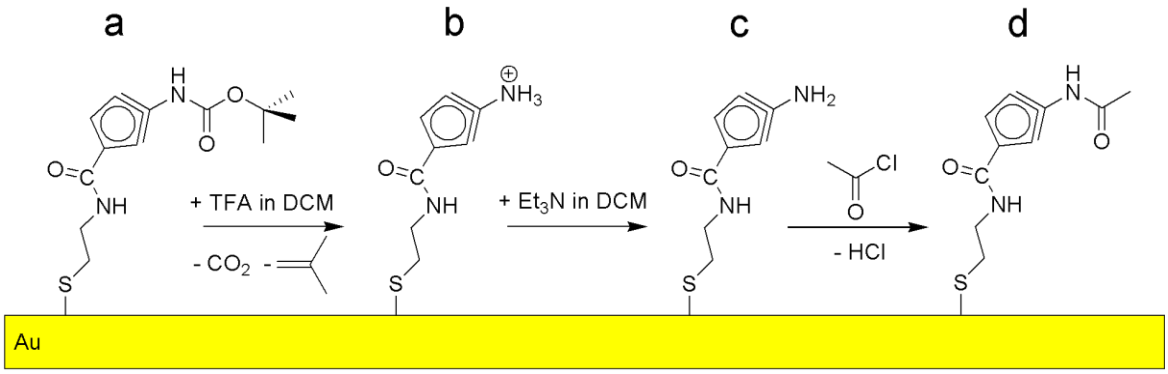

Figure 2.6: The (a) Fc amino acid derivative on a gold surface after (b) Boc deprotection, (c) deprotonation and (d) exposure to acetyl chloride.

Anodic peak integration of the film CV scan pre- and post-TFA treatment (*i.e.*, prior to simulant exposure) in aqueous 2.0 M $NaClO_4$ (pH = 6.1) electrolyte revealed a decreasing signal (Fig. 2.7 insert, *cf.* blue *vs.* black traces). This is the result to a reduction in the number of Fc molecules (as signal is proportional to the electrochemical probe concentration) either by the removal of the Fc component or of the molecule as a whole. The post-TFA CV scan (*i.e.*, stage of film depicted in Fig. 2.6b) increased the deterioration of the film possibly due to molecule instability followed by film decomposition.

Simulant reactivity with the deprotected-deprotonated Fc amino acid derivative system (Fig. 2.6c) was unsuccessful and no apparent changes in the CVs were observed. Solutions of 1 mM 2-chloroethyl ethyl sulfide and diethyl cyanophosphonate (2-CEES and DECP simulants of blistering sulfur mustard and Tabun nerve agent respectively) diluted in either MilliQ water, aqueous 2.0 M $NaClO_4$ electrolyte or DCM were unsuccessful in producing a signal shift when exposed for 1 min to deprotected-deprotonated films. The electrochemical system reacted, however, when tested with a 1 mM acetyl chloride (CH_3COCl) in DCM solution for 1 min exposure (Fig. 2.6d). This may indicate a kinetic issue in which the simulants 2-CEES and DECP are slower to react than CH_3COCl requiring longer incubation.

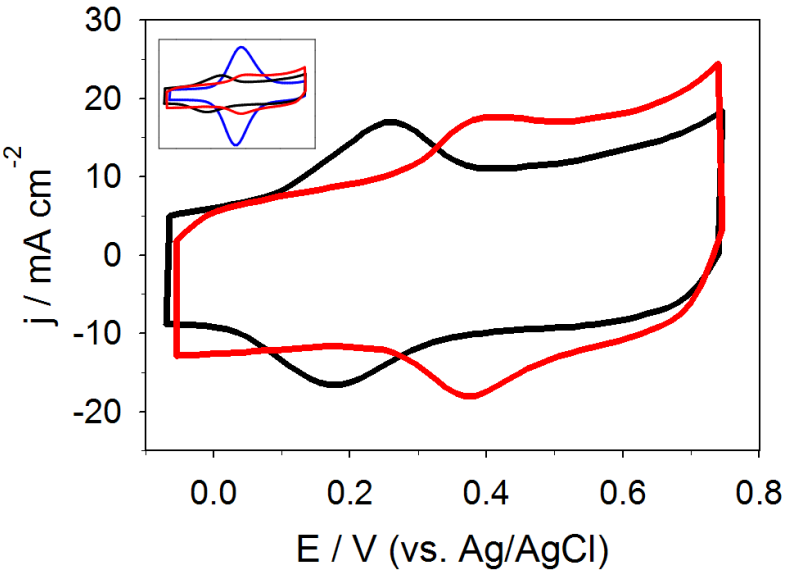

State	Γ (Å²)	E° (mV)	ΔE_p (mV)	i_{pa} / i_{pc}
Protected (blue)	52 (±2)	360 (±7)	31 (±4)	1.00
Deprotected (black)	195 (±20)	271 (±6)	60 (±15)	1.17
Reacted (red)	633 (±33)	388 (±7)	31 (±8)	0.93

Figure 2.7: CV scans of $[(BocHN)Fc(CO)CSA]_2$ films electrodeposited onto 50 µm gold microelectrodes deprotected (black trace) and exposed to 1 mM acetyl chloride in DCM (red trace). Insert shows the protected form (blue trace). The accompanying table describes the footprint or surface coverage (Γ), the formal potential (E^o), the peak position difference (ΔE_p) and the current ratio (i_{pa}/i_{pc}). Errors are the standard deviations from three measurements. CV scans recorded at 100 mV/s in 2.0 M $NaClO_4$ utilizing a Pt wire as the counter electrode.

Fig. 2.7 shows the CV scans of the three stages (*i.e.*, Boc-protected, deprotected and exposed) of the Fc amino acid derivative film reacting with 1 M CH_3COCl. The Γ of the film thins significantly as the ME is exposed to each stage of the reaction process. For example, when the film is Boc-protected, each molecule requires an area of 52 ± 2 $Å^2$ on the gold surface. Once the film has been deprotected and reacted, this area has increased to 633 ± 33 $Å^2$ for a *complete* molecule. Again, the deprotection and simulant exposure processes could be responsible for the

removal of the Fc only leaving behind the gold-bound alkyl chain part of the Fc amino acid derivative.

The E^o of the Boc protected film is 360 ± 7 mV while its formal potential shifts cathodically for the deprotected form at 271 ± 6 mV (Fig. 2.7). This could be explained as the Boc group is a large ligand that hinders electron transfer, thus more energy is required by the Fc molecule to perform redox processes. Once Boc is removed, less energy is required to oxidize the molecule and a cathodic shift is observed on the CV scan. The E^o shifts anodically at 388 ± 7 mV once the acetyl group reacts with the Fc amino acid derivative film.

The ΔE_p and i_{pa}/i_{pc} values for the protected film are 31 ± 4 mV and 1.00, respectively, indicative of a surface-bound reversible film (Fig. 2.7). This cannot be said of the deprotected film. The deprotected form shows quasi-reversible characteristics as its ΔE_p is 60 ± 15 mV and its current ratio is 1.17. This could be due to the reactive form of the amino group which decreases the stability of the film until it reacts with CH_3COCl. In its reacted form, the film returns to a surface-bound reversible film characteristic as its ΔE_p is 31 ± 8 mV and its current ratio is 0.93.

Conclusions. This chapter describes the results of the Fc amino acid derivative $[(BocHN)Fc(CO)CSA]_2$. We have shown that electrodeposition is an effective methodology to immobilize this molecule onto Au microelectrodes. Films formed *via* electrodeposition were more stable, produced higher surface coverage values, were more reproducible and saved preparation time compared to the potential-unassisted solution deposition method. This is in agreement with earlier results on unrelated Fc-peptide disulfides.[74]

The film electrochemical response after the process of Boc-deprotection turned out to be a harsh step to the film as it led to a decrease in signal intensity due to, most likely, the loss of the

Fc redox probe. A less likely scenario is the removal of the entire molecule off the substrate. Clearly, a better method needs to be developed in order to deal with this issue. The remaining signal after deprotection was strong enough to observe a cathodic shift compared to the Boc-protected formal potential of the CV scan. Furthermore, the deprotected film was shown to react with 1 mM acetyl chloride when exposed for 1 min, producing an anodic shift compared to the deprotected formal potential. Unfortunately, when exposed to the CWAs simulants 2-CEES and DECP, no such shift was observed. We hypothesize that the reaction for the Fc amino acid molecule with either of the simulants requires longer than the 1 min incubation time tested.

CHAPTER 3
SILVER NANOPARTICLE SYSTEM

Nanoparticles (NPs) are particles in the size of nanometer scale. Although not technically correct, it is generally accepted in the scientific community that the term NPs is applied to particles sizes from 1 to 100 nm in diameter.[76-78] At this size scale, the physical properties of materials differ from their bulk counterparts. For instance, iron aluminide (FeAl) is a non-magnetic and brittle material in its bulk powder form while FeAl NPs of 6–9 nm become ferromagnetic and malleable.[79,80] Another example is gold, which in its bulk state is considered chemical inert.[85] Au NPs, on the other hand, possess catalytic activities at 3–5 nm such as for the oxidation of carbon monoxide (CO)[83] and for the catalytic decomposition of malodourous compounds such as ammonia (NH_3) and trimethylamine (Me_3N) commonly found in restrooms.[81]

The current areas of research for NPs are broad encompassing areas in the biological, chemical and physical sciences. In the biological fields, NPs have shown to be effective in anticancer treatments, as antibacterials and drug delivery systems.[83] In the detection field, they have been used as part of biological sensors systems when accompanied by enzymes and/or nucleic acids and as chemical sensors in the form of Pd nanowires for the detection of H_2.[84] A prime example of NPs use in everyday life is as additives in sunscreen lotion. For instance, zinc oxide (ZnO) and titanium dioxide (TiO_2) are two compounds that do not chemical decompose under UV radiation.[85] This property makes them excellent candidates as additives on sunscreens. Interestingly, large-particle inorganic oxide formulations are opaque in colour, in turn lacking cosmetic acceptability; however, in NP-size form (*i.e.*, 26–30 nm), these oxides show superior UV blocking properties and are transparent when spread on the skin surface making them visually acceptable by sunscreen users.[85]

3.1. Nanostructures *versus* Bulk Materials

The examples described in the previous section, illustrate the unique properties of NPs when compared to bulk materials. Thus, the interest of NPs resides in the fact that their physical properties differ from those of their bulk analogues.

In order to understand or rationalize the physical properties characteristic of nanostructures, their energy level structure needs to be discussed.[86] The reasoning behind this is that nanostructures are linking the atomic world with that of the bulk material. One way to analyze this notion conceptually is to start with a bulk piece of material and gradually reduce its size.[86,87] It is expected that, during this process, as the starting bulk material becomes smaller and smaller, a stage is reached in which its properties cease to exist at the atomic level. In other words, the atomic particles (*i.e.*, electrons and nuclei) do not behave as the smaller copy of the corresponding bulk solid.[87]

At the atomic level, atoms show discrete energy levels for their electrons. These discrete energy levels are known as atomic orbitals. When atoms bind to form molecules, the atomic orbitals combine to form molecular orbitals. In methane (CH_4), for instance, the central C contains 4 valence electrons each in a single sp^3 hybridized atomic orbital (originated from its 2 paired electrons in the 2*s* atomic orbital and 2 unpaired electrons in the 2*p* atomic orbital) each bound to the *s* electron of each H atom.[86] In the binding process, bonding (σ) and anti-bonding (σ*) orbitals are created.[86] Since there are 8 atomic orbitals invested in the bonding (*i.e.*, 4 from C in the form of sp^3 hybridized atomic orbitals and 4 for each bound H in the form of *s* atomic orbitals), there are 8 molecular orbitals created. Also, from Pauli's Exclusion principle, a maximum of 2 electrons can occupy an orbital. These newly created orbital are: 4 lower energy σ orbitals containing all the electrons and 4 σ* orbitals of higher energy containing no electrons. For even larger molecules, the same approach applies. However, as the number of molecular

orbital increases, the average energy gap between adjacent molecular orbitals must decrease.[88] At the same time, the gap between σ and σ* orbitals also decreases until a continuum energy level occurs,[88] for instance, the case of a system describing a bulk material in which an "infinite" number of bonds are formed (*i.e.*, an infinity bulk size is assumed). In other words, the energy structures of a bulk solid no longer consists of discrete energy levels, but rather of broad energy bands,[86] effectively describing a transition from orbitals to bands.[88] This is known as the band theory. For a bulk, band theory results in two bands: the valence band of lower energy, which contains the electrons, and the high-energy conduction band. These bands are divided by an energy band gap (Fig. 3.1).

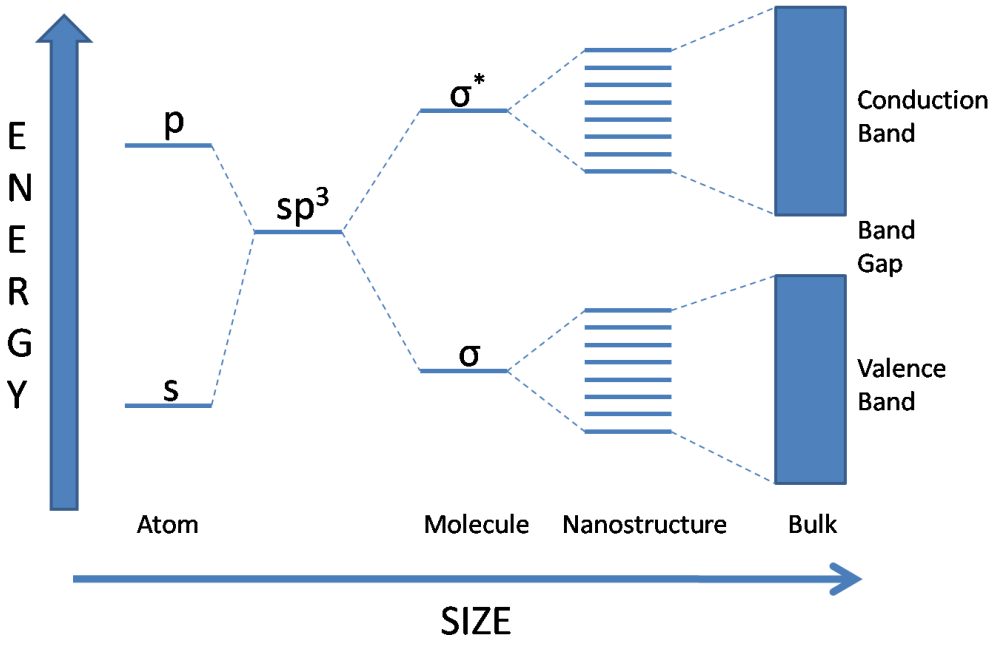

Figure 3.1: Graphical representation of the electronic energy levels of matter as they increase in size (from left to right). At the atomic level, electrons show discrete energy levels known as atomic orbitals. At the molecular level, atoms bind forming separated electronic levels called molecular orbitals. In a bulk material, the electronic levels are formed by continuous broad energy bands. For nanostructures, the electronic levels can be regarded as a hybrid between molecules and bulk material.[86.] Adapted from ref. 89.

The assumption applied for a bulk solid using band theory does not apply to nanostructures. This is clear as the assumption of "infinite" number of bonds, as is the case for a bulk solid, is no longer valid. The electronic structure of nanomaterials is an intermediate stage between the discrete levels of an atomic system and the continuous band structure of a bulk solid.[86] As illustrated in Fig. 3.1, the energy levels in nanostructures are discrete; however, these levels are more numerous and their spacing is smaller than the corresponding atomic or molecular systems.[89] At the same time, band theory can also be applied to describe the peculiar energy levels of nanostructures. For instance, in nanostructures, the highest occupied atomic orbitals of an atom interacting with other atoms present in the nanostructure form the valence band; the lowest unoccupied levels combine to form the conduction band; and, the energy difference between the valence band and the conduction band form the band gap.[86]

Another difference between nanostructures and bulk material is the number of atoms on the surface. By simple deduction, one can imagine that the percentage of surface atoms to interior atoms for a bulk material is very low. As particles get smaller and smaller, this percentage shifts due to a lower number of atoms per unit particle. This is elegantly shown by Schmid's experiments[90] in which he used Au atoms to form cluster of different sizes (see Fig. 3.2). For instance, it takes 13 metal Au atoms for form a single-shell cluster which contains 92% of its atoms on the surface. On the other hand, if the size of the cluster increases by 5 shells, the number of atoms forming the cluster increases to 561 and its surface atoms decreases to 45%.

The effect of a higher number of atoms at the surface of particles has been linked to catalytic performance. By definition, a catalyst modifies a chemical reaction by affecting the rate of the reaction. A heterogeneous catalyst (*i.e.*, a catalyst present at a different phase than the reactants) activity is proportional to the overall specific area per unit volume.[91] However, decreasing the

size of particles does not necessarily translate to higher catalytic activity. For example, as previously mentioned, the catalytic activity of metal Au NPs has been found optimal at 3–5 nm for the oxidation of CO.[82] On the other hand, the optimal photo-oxidation of phenol in water by the semiconductor titania (TiO_2) NPs is 25–40 nm.[82] In both cases, decreasing the size below that of the optimal value shows diminishing catalytic activity. Although size optimization between metal *versus* semiconductor particles differs greatly, efforts explaining these variations have been based on their electronic band structure difference. Unfortunately, there is no current electronic energy band understanding to explain optimal catalytic behaviour at a specific size.[92]

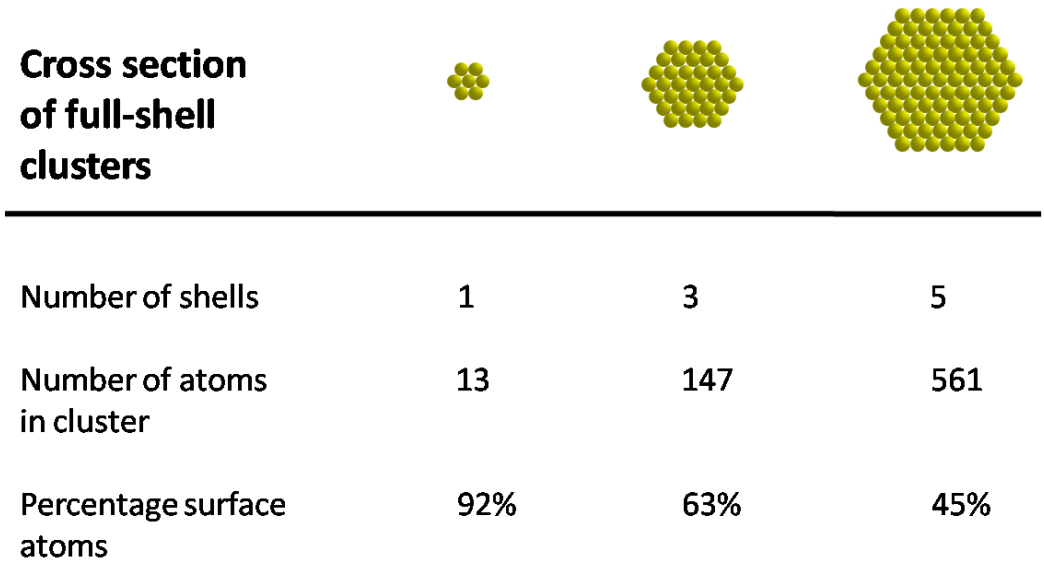

Figure 3.2: Gold clusters of different sizes showing how the number of shells relates to the number of atoms in the cluster and to the percentage of atoms at the surface of the cluster. Adapted from ref. 90.

3.2. Electrochemistry of Nanostructures

The examples presented in the previous sections, indicate that the ability to control material dimensions to the nanometer scale would result in unique surface chemistry events not observed in bulk systems.[93,94]

For years the use of silver NPs and roughened surfaces with nanodimensioned features have been used to generate SERS (Surface Enhanced Raman Spectroscopy) and SEIRA (Surface Enhanced Infrared Adsorption-Reflectance) active surfaces where the Raman or infrared spectroscopy of species on the Ag surface can be monitored *in situ* as electroanalysis is being conducted. The spectroscopy allows for species that are electrochemically generated on Ag surfaces to be identified. Although this technique is a powerful approach to understanding products and reaction paths, evidence is accumulating that the chemistry of nanodimensioned Ag is size-dependent. For instance, Burke has demonstrated the presence of surface active states that preferentially form types of β-oxides.[95] These oxides only appear upon formation of nanodimensioned structures on roughened polycrystalline Ag electrode surfaces as a result of anodic oxidation *via* electrochemical etching (*i.e.*, surface disruption) in high pH electrolyte conditions.

The size of the NPs affects their catalytic properties during electrochemical reduction studies for a particular compound or metal. In a combined scanning tunnel microscopy (STM)-electrochemical experiment, it has been shown that palladium NPs increase their catalytic reduction reactivity of hydrogen (*i.e.*, H evolution reaction) by two orders of magnitude when the number of Pd shells on the NP decrease from 10 to 2, effectively decreasing their size from 200 to 6 nm.[96] A similar trend was obtained by studying Au nanoelectrodes and the H evolution reaction. By decreasing the working Au electrode size from 800 to 10 nm, it was determined that the current density (and thus the degree of catalytic activity) did not deviate

much in the range from 800 to 30 nm.[92] The current density significantly increased, however, when the Au electrode reached below 30 nm, specifically in the 15 to 10 nm range. It has been postulated that as the size of the catalyst surface decreases, it approximates the size of the reaction site needed for adsorption of the reactants, effectively eliminating unused surface and maximizing reaction site distribution.[92] These results indicate that nanodimensioned structures used as working electrodes could potential increase the sensitivity of the system.

3.3. The Silver Nanoparticles on Indium Tin Oxide System

In electrochemistry, decorating electrodes with nanomaterials of different metals, where each set of nanomaterials behaves like a collection of nanoelectrodes of that metal, has recently been demonstrated as a viable way of effecting combinatorial-type electroanalytical analysis on a single electrode.[97] Fabrication of such modified electrodes has been carried out using electroless deposition of NPs,[97] by electrochemical immobilization of solution phase NPs,[98] by nanostructure synthesis on electrode surfaces utilizing the double-pulse method,[99] and by electrochemical/chemical deposition methods.[100] An alternative approach is the direct deposition of gas-phase NPs onto conducting substrates.[101] Sputtering-based sources have recently become commercially available allowing for the generation of NPs made of any metal in the periodic table. As a way of fabrication electrodes, gas-phase deposition has the advantage of ligand-free NP fabrication effectively creating direct contact between the NPs and the electrode substrate. Furthermore, the particle density on the substrate surface can be controlled along with the spacing between particles by adjusting deposition times.[101]

This electrochemical system consisted of gas generated naked Ag NPs deposited on indium tin oxide (ITO) glass templates.

3.4. Results and Discussion

3.4.1. Basic Characterization of Silver Nanoparticles.

The topography of NP-decorated ITO electrodes was investigated by scanning electron microscopy (SEM). Fig. 3.3 shows a typical SEM scan of the NP-decorated ITO surface in which the NPs are deposited as a thin film with relatively constant spacing. The SEM image shows sub-10 nm NPs. However, due to size limitations associated with this technique, previous STM experiments under the same deposition conditions confirmed a size of 3.0 ± 0.5 nm with interparticle separations (centre-to-centre) of *ca.* 10 nm.[102]

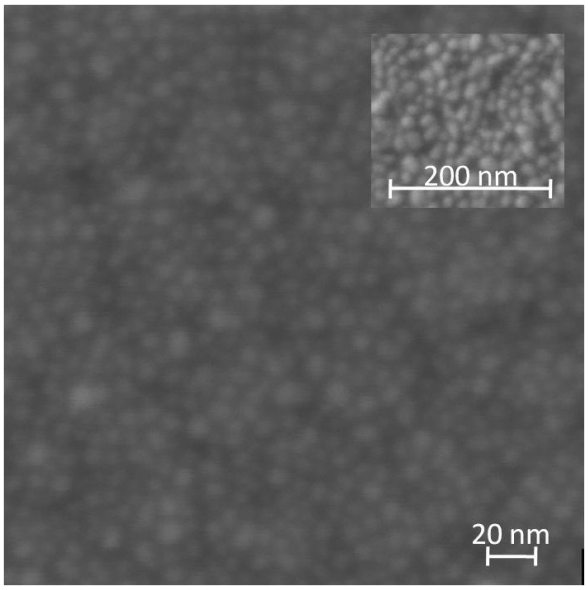

Figure 3.3: SEM images of silver NPs on ITO electrode. The insert shows a lower magnification. Due to resolution limitations, the SEM image shows larger particles that previous STM studies (3.0 ± 0.5 nm by STM[102]). SEM performed on a Leo 1540 XB SEM CrossBeam Workstation.

The relative constant interparticle spacing can be varied by changing deposition time. This was demonstrated in NP deposition time experiments on highly ordered pyrolytic graphite (HOPG) substrates analyzed by atomic forced microscopy (AFM) as shown in Fig 3.4.

Interparticle spacing becomes particularly useful as a way to minimize interactions between adjacent proteins, for example, when using NPs as active sites on the electrode surface to anchor and/or detect such macromolecules.[103]

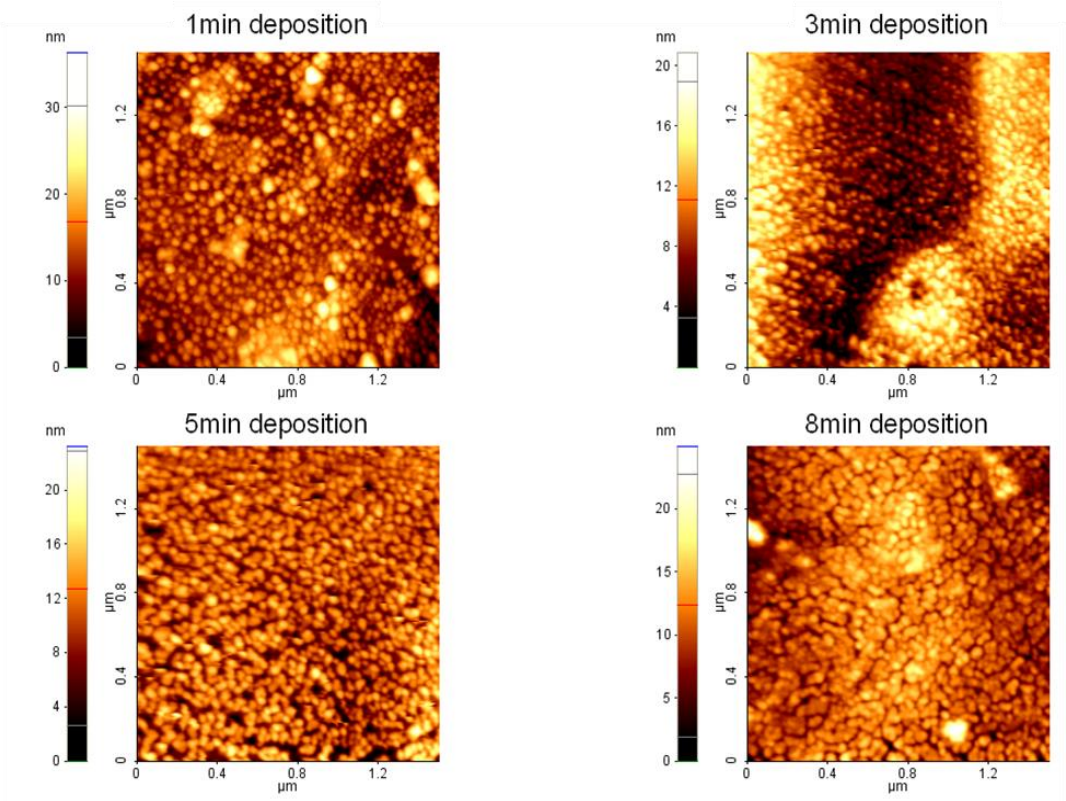

Figure 3.4: AFM images of silver NPs on HOPG substrates. NPs were deposited for 1, 3, 5 and 8 min on different substrates. At 1 min deposition time, individual particles are visible. As the deposition time increases, the spacing among the NPs decreases. At 8 min, individual particles are no longer distinguishable forming a film on the substrate. AFM performed on a PSIA model XE-100.

3.4.2. Silver Nanoparticles Redox Chemistry in KOH.

Fig. 3.5 shows a comparison of typical CV scans of bulk polycrystalline Ag and of Ag NPs/ITO, both recorded in 8.0 M aqueous KOH. This condition was chosen based on scientific literature on polycrystalline Ag electrochemistry,[104] later the vital importance of such

condition will be discussed. It is important to note that during cycling at these conditions, the NP-decorated electrode displayed signal instability not observed in the bulk Ag electrode system. Continuous cycling led to a continual decrease in peak height and to the shifting of peak intensities. This effect is minimized, however, when lower supporting electrolyte concentrations were used (*e.g.*, 100 mM KOH). This effect is mentioned several times throughout this chapter. The same labelling scheme utilized by Burke for the polycrystalline results (Fig. 3.5a) has been adopted[95] (with the exception of *x* and *y* peaks). Although there are peaks in the NP-decorated electrode analogous to the bulk system, the two CV scans are significant differently.

The CV of polycrystalline Ag displays a series of anodic events labelled A_1, A_2, and A_3 (Fig. 3.5a) that were attributed to oxidation of $Ag \rightarrow Ag^+$. A_4 corresponds to oxidation of Ag^+: $Ag_2O \rightarrow AgO$. In the cathodic sweep, C_2 is the redox couple of A_4 (*i.e.* $AgO \rightarrow Ag_2O$) and C_1 is the redox couple of peaks $A_1 - A_3$ (*i.e.* $Ag^+ \rightarrow Ag$). The exact nature of the oxide species produced by the three signals $A_1 - A_3$ is not yet clear but likely involves hydroxides as well as Ag_2O.[95,104] There are also two small, yet visible, peaks observed during the anodic sweep at *ca.* 0.72 V (denoted *x*) and at *ca.* 0.47 V in the cathodic sweep (denoted *y*).

The CV of Ag NPs/ITO (Fig. 3.5b) is less complex than that of the bulk counterpart. The NPs CV scan has a number of known anodic and cathodic features,[105] that can be assigned based on a comparison with bulk Ag literature data. The anodic signals A_1, A_2, and A_3, observed in the bulk phase, are replaced by a single feature at 0.16 V, which is close to the signal for A_2 in bulk Ag. A second anodic peak in the Ag NPs CV at 0.72 V is near bulk *x*. The cathodic sweep shows two peaks appearing at 0.42 and at -0.35 V. The peak at 0.42 V is attributed to *y* while the signal at -0.35 V is a feature which Burke designated C_0.[95] In short, except for C_0, all peaks observed

in the Ag NPs are present in the bulk CV scan. The relative importance of these processes in each system is different as reflected in the difference in the relative peak heights (*cf.* A_2 *vs.* A_3).

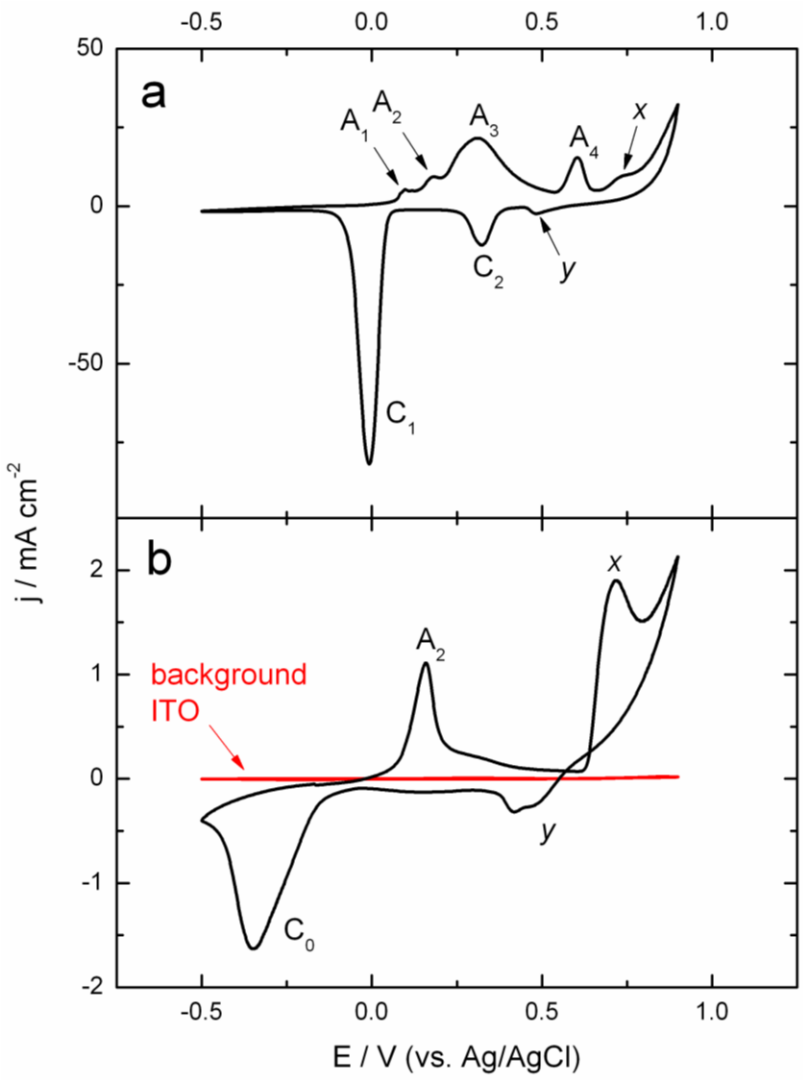

Figure 3.5: CV scans of (a) polycrystalline silver, (b) silver NP-decorated ITO and of background ITO (red trace in b) in degassed 8.0 M KOH at 150 mV/s between -0.5 and 0.9 V *vs.* Ag/AgCl. During the anodic sweep, peaks A_1, A_2 and A_3 are attributed to the oxidation of Ag to Ag^+ at several stages. Peak A_4 corresponds to the oxidation of Ag^+ to Ag^{2+}. Peak *x* is characteristic of an oxidation process by nanostructures. During the cathodic sweep, peak *y* is characteristic of a reduction process by nanostructures. Peak C_2 is the reduction of Ag^{2+} to Ag^+ while C_1 is the reduction of Ag^+ to metallic Ag. Peak C_0 is attributed to β-oxide reduction formed preferentially on nanostructure surfaces.

C_0 is associated with the reduction of β-oxides,[95] and is linked to multilayer oxide growth in a number of metals (Au,[106] Pt[107] and Ag[95]). In the case of Ag, the β-oxide deposits on top of a thin film of compact α-oxide layer right on the metal surface.[95,106] The compact α-oxide is usually associated with AgOH, Ag_2O and AgO while β-oxide has been associated with different hydrous composition variations, for example $Ag(OH)_n(H_2O)_m$.[95] Charge transport through such hydrated hydroxides is thought to be kinetically hindered, which results in characteristically broad peaks in the CV scans observed for C_0. Presumable reduction of the Ag β-oxide is sluggish due to the poor contact with its metal surface.[95] An interesting electrochemical feature of β-oxide complexes is that the C_0 peak is only observed on *roughened* polycrystalline Ag electrodes following extensive anodic oxidation at high electrolyte concentration, which leaves nanodimensioned structures on the surface. Essentially C_0 can be viewed as an indicator for the presence of nanostructured Ag surfaces.

In our experiments of Ag NPs on ITO, we observe a C_0 peak for β-oxide reduction (Fig. 3.5b). As has been reported for bulk systems, C_0 appears only if the potential window scan exceeds an upper voltage value near A_4.[95] This suggests that, in our nano system, C_0 corresponds to the reduction of β-oxides generated by applying voltages near peak *x*. As confirmation, a fresh NP-decorated electrode was cycled in a smaller potential window (*i.e.*, -0.5 to 0.3 V, Fig. 3.6). In this CV scan, peak C_0 is not observed in the cathodic sweep but a peak at -0.11 V, coupled to A_2, is present. It has also been reported that in bulk Ag, peak A_2 is enhanced by electrochemical cycling due to surface disruption,[95] an observation that connects this peak to nanodimensioned structures on the polycrystalline electrode surface. Furthermore, as previously stated, the anodic peak at 0.16 V observed in our large potential window Ag NPs/ITO CV scan (Fig. 3.5b), is closer in potential value to bulk A_2 on our polycrystalline

CV scan than to either A_1 or A_3 (Fig. 3.5a). This suggests nano-imperfections on the polycrystalline surface give rise to this peak. When generation of β-oxides is precluded, by limiting the upper voltage of the anodic sweep, surface oxides (*i.e.*, α-oxides) necessarily remain unoxidized on the ITO surface. The presence of these oxides is thought to manifest the appearance of C_1 at -0.11 V in Fig. 3.6, instead of C_0 dominant in the large window (Fig. 3.5b).

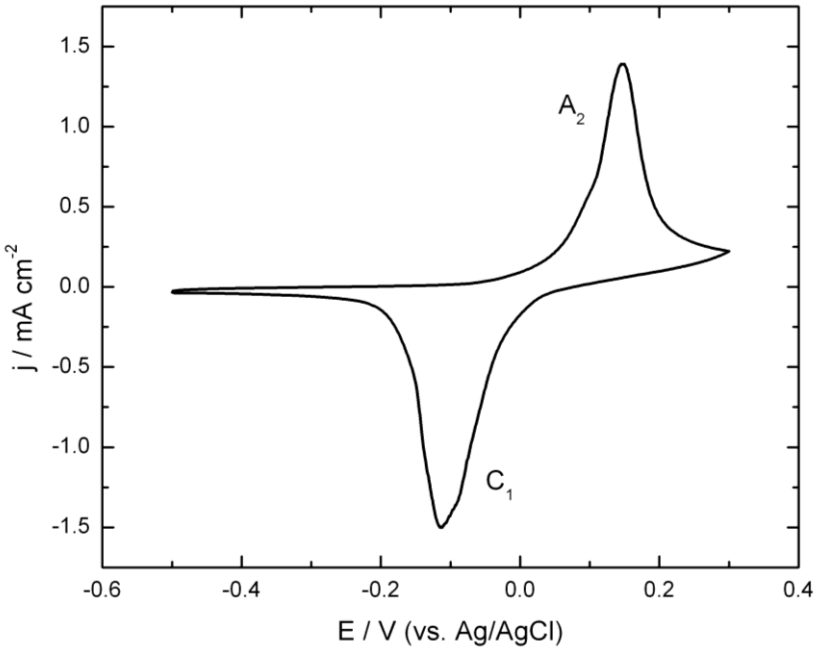

Figure 3.6: CV scan of silver NP-decorated ITO in degassed 8.0 M KOH at 150 mV/s between -0.5 and 0.3 V *vs.* Ag/AgCl. This potential window only allows for the formation of Ag^+ at A_2. Consequentially, C_1 corresponds to the reduction to Ag^+ back to metallic Ag.

A second feature of the Ag NPs CV scan distinct from the bulk electrode scan (Fig. 3.5b and 3.5a, respectively) is the crossings of the anodic curve during the negative cathodic sweep. Such crossing is hysteresis characteristic of impeded charge transport. Typically, hysteresis is the result of low electrolyte concentration[108] due to the slow mass transport of ions to the redox active surfaces. For instance, the crisscross effect has been observed by others in 0.1 M KNO_3

electrolyte with Ag NPs.[98] In our case, however, the supporting electrolyte concentration is high at 8.0 M KOH and this effect is unlikely. A more plausible explanation to our hysteresis effect is that the charge transfer is impeded by the presence of β-oxides in the electrochemical double layer around the NPs. Both the β-oxides and the nano-dimensions of the Ag surfaces likely impact the charge transport. Remarkably, the hysteresis effects observed at 8.0 M KOH is minimized with lower electrolyte concentrations opposite to observations in hysteresis caused by impaired mass transport of electrolyte ions.

A third characteristic of NP-decorated electrodes distinct from bulk metal electrodes is the formation of aggregates on the ITO surface. In this study, naked Ag NPs were deposited directly onto ITO without the aid of interlinking molecules. Accordingly, electrochemical cycling of NP-decorated electrodes in 100 mM KOH electrolyte solution was found to cause some aggregation of particles. This phenomenon was observed regardless of supporting electrolyte concentration. This effect is shown in Fig. 3.7 in which a significant amount of particle aggregation has occurred compared to Fig. 3.3 (*i.e.*, uncycled sample). This observation demonstrates that aggregation of NPs is part of the chemistry occurring in these systems. The aggregation, however, has no obvious effect on the electrochemistry observed. In general, there is no observable correlation between extent of aggregation and the electrochemical cycling history of the sample. The results suggest that, although the NPs have aggregated, they have not coalesced and therefore retain their identity as distinct NPs on the ITO surface. Careful inspection of Fig. 3.7 suggests that each aggregate consists of discrete individual NPs.

Ostwald ripening processes cannot be excluded.[109] Continuous electrochemical cycling of the Ag NPs on ITO is expected to cause partial dissolution and redeposition of Ag. In this process, the growth of larger particles at the expense of smaller ones is favoured due to the lower surface

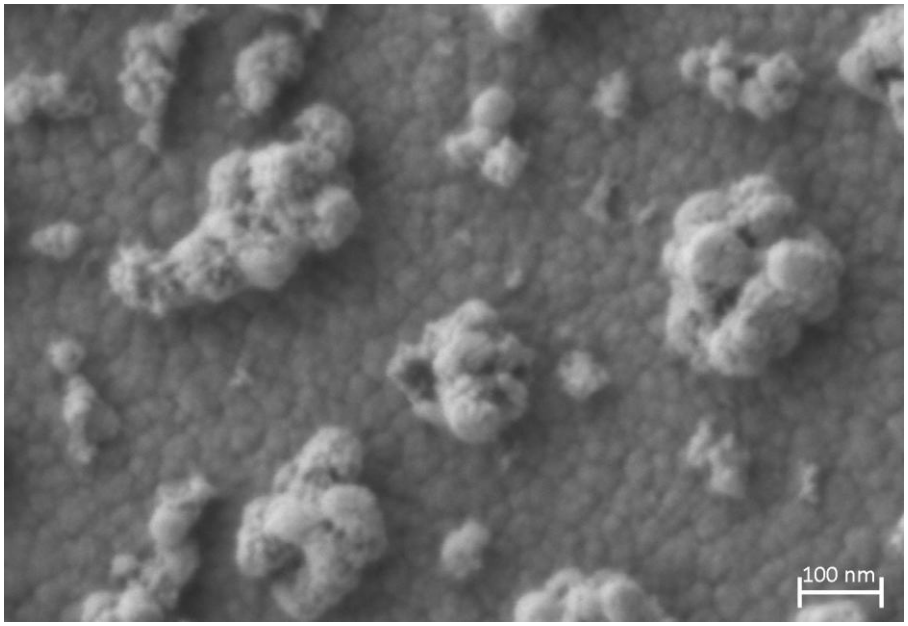

Figure 3.7: SEM images of silver NP-decorated ITO electrode after electrochemical cycling in degassed 100 mM KOH. Silver aggregates are observed on the ITO substrate.

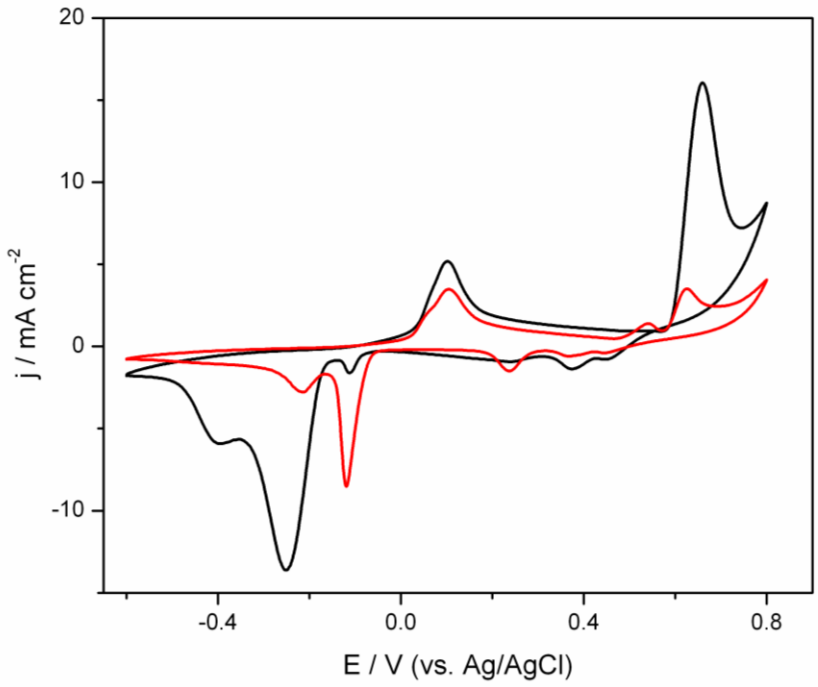

Figure 3.8: CV scans of silver NP-decorated ITO in degassed contaminant-free 8.0 M KOH at 150 mV/s *vs.* Ag/AgCl. At high-numbered cycles, the CV scans show the surface oxide peak at *ca.* -0.17 V. Black trace represents the 55th cycle while the red trace is the 80th cycle.

energy associated with larger NPs.[110] Continuous electrochemical cycling could therefore cause a significant change in the NP size distribution and may lead to an eventual loss of NPs. The use of KOH as supporting electrolyte in the present study helps minimize Ag loss due to dissolution, as AgOH is extremely insoluble, in turn, reducing the Ostwald ripening process. However, under extreme experimental conditions (*i.e.*, 80th cycle in contaminant-free 8.0 M KOH), loss of NP-type CV and appearance of bulk-like CV were observed as expected of a ripening/annealing process (Fig. 3.8).

3.4.3. Effects of Chemical Warfare Simulant Additives on the Electrochemistry of Silver Nanoparticles.

Due to the differences in their properties from bulk Ag, we anticipated differences caused by the adsorption or chemisorption of small molecules onto the NPs. To test this hypothesis, Ag NPs/ITO electrodes were exposed to supporting electrolyte containing DECP or 2-CEES, simulants of the CWAs Tabun nerve agent and blistering sulfur mustard respectively (see Fig. 1.1 in Ch. 1). It is worth noting that these species have no redox chemistry that can be exploited for detection.

Diethyl cyanophosphonate: The addition of DECP at a final concentration of 1 mM to a 100 mM KOH electrolyte solution has a significant effect on the electrochemical behaviour of the Ag NPs as is shown in Fig. 3.9a. While there are no new redox signals associated with redox processes involving DECP, there is an immediate and significant decrease in the signal intensity of Ag NP-based redox events described earlier, consistent with loss of redox active surface sites. Note that, at these conditions, the signal indicating β-oxide formation is minimal (*i.e.*, C_0) and the electrochemical signal is stable in the absence of DECP. The result suggests dissolution of Ag as the cause of signal loss. This concurs with the SEM images of the DECP-exposed sample

in Fig. 3.9b. The image reveals an almost bare ITO substrate with a greatly reduced Ag aggregate population. As DECP hydrolyzes readily in aqueous base, the formation of CN^- ions provide a plausible mechanism for dissolution of Ag. CN^- is the standard titrant used in Liebig's method of silver analysis, which relies on the high solubility of $Ag(CN)_2^-$ anions.[111] Formation of such anions would result in dissolution of Ag leading to loss of NPs and aggregates, consistent with observations. Electrochemistry is not required for this reaction to occur; however, it can be utilized for detection. Although analogous chemistry can occur on bulk Ag electrodes, the

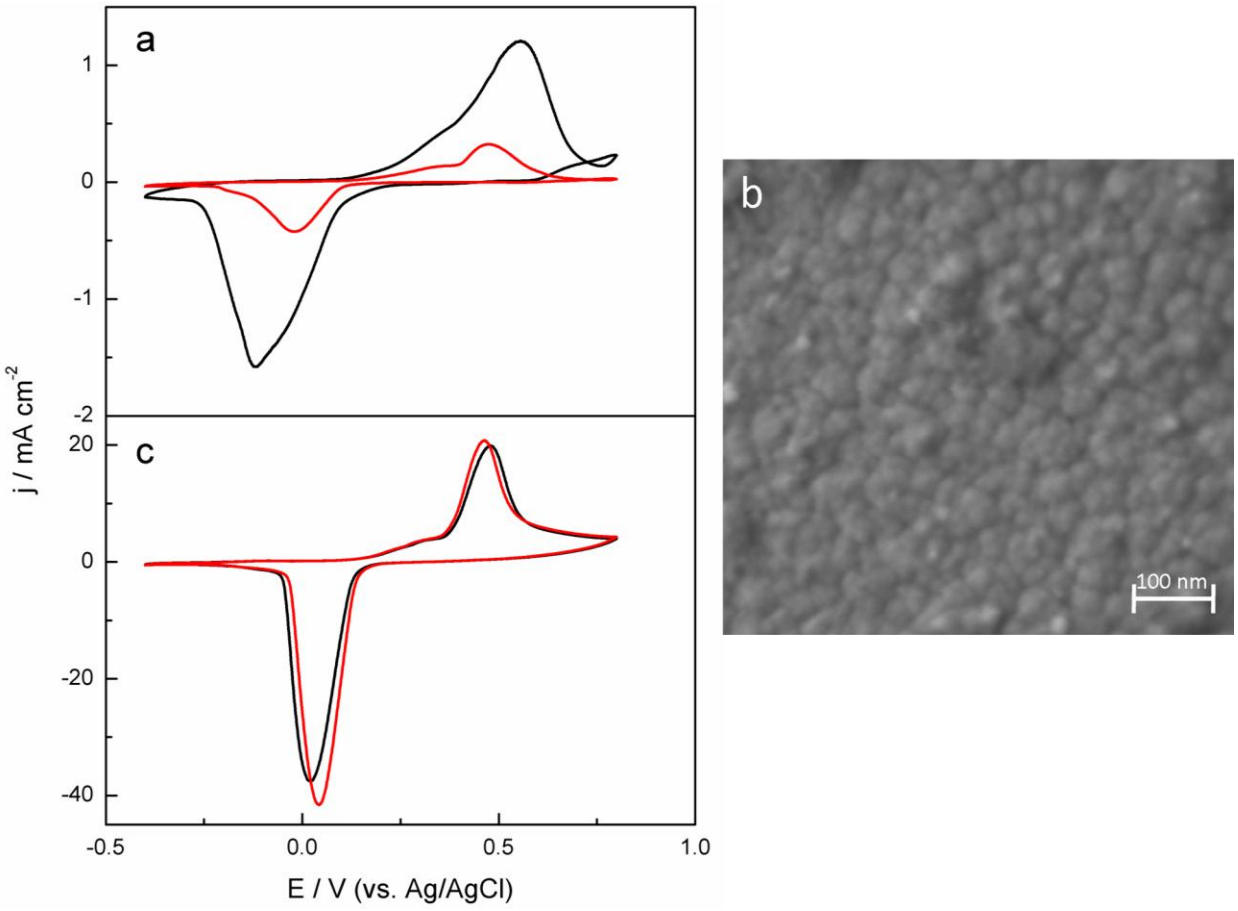

Figure 3.9: (a) CV scans of silver NP-decorated ITO exposed to 1 mM DECP, (b) its SEM image, and (c) CV scans of bulk polycrystalline silver exposed to 5 mM DECP. Black scans represent pre-exposure conditions while the red scans correspond to 15 cycles post-exposure. Experiments conducted in degassed 100 mM KOH at 150 mV/s scan rate between -0.4 and 0.8 V *vs.* Ag/AgCl.

NP-decorated electrode is much more sensitive due to its high surface area and to the low metal mass present, which facilitates rapid dissolution of Ag, resulting in a rapid decline of CV signal. As seen in Fig. 3.9c, the CV scan of polycrystalline Ag in 100 mM KOH exposed to 5 mM DECP does not involve, either decline in signal intensity nor peak shifting and the presence of DECP goes undetected.

2-Chloroethyl ethyl sulfide: In contrast to nerve agents, the CWA sulfur mustard is much slower to hydrolyze in basic conditions, due in part to its poor aqueous solubility.[112] The same argument applies to its corresponding simulants. For example, standard procedures for sulfur mustard destruction, requires 10% W/V KOH-methanol solutions for 24 h. The relatively inert electrochemical nature of sulfur mustard is reflected, in this study, with 2-CEES and is illustrated in Fig. 3.10. Addition of 1 or 5 mM 2-CEES to Ag NP-decorated electrodes in 100 mM KOH electrolyte had no effect on their electrochemical behaviour even after repeated cycling (see Fig. 3.10a). However, in the presence of β-oxides (*i.e.*, Ag NP-decorated electrode at 8.0 M KOH), the effect of 1 mM 2-CEES is dramatic as shown in Fig. 3.10b.

After 2-CEES addition, the C_0 signal, characteristic of β-oxides, is significantly diminished in magnitude and the signal at -0.15 V, characteristic of surface oxides, increases in intensity. Clearly, there is a requirement for high electrolyte concentration, and thus of extensive β-oxide formation in order to detect 2-CEES. The loss of β-oxides is consistent with the known chemistry of sulfur mustard which readily reacts with Ag NP oxides.[113,114] The fact that β-oxides form preferentially on nanostructured surfaces, as previously discussed, may explain why analogous chemistry is not observed on bulk Ag surfaces as shown in Fig. 3.10c.

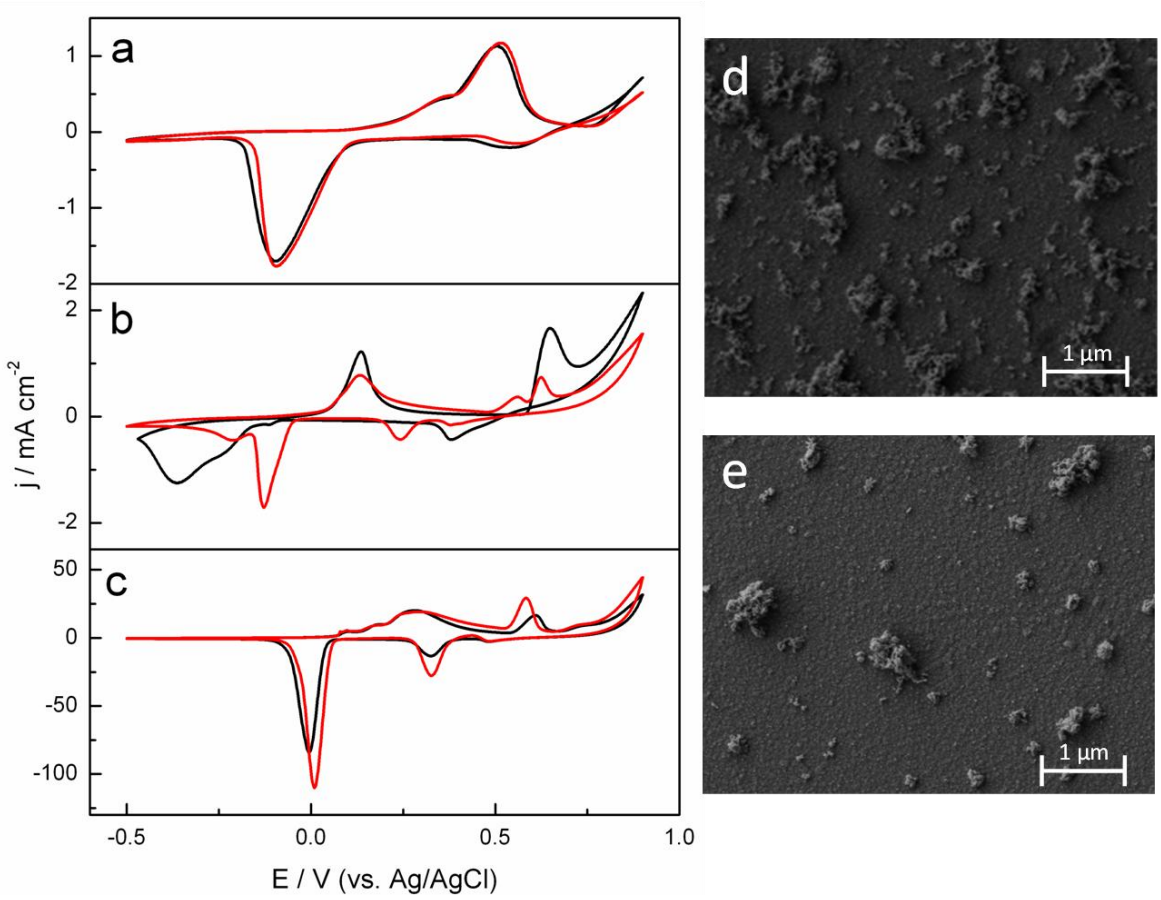

Figure 3.10: CV scans of silver NP-decorated ITO exposed to (a) 1 and 5 mM 2-CEES in degassed 100 mM KOH and to (b) 1 mM 2-CEES in degassed 8.0 M KOH. (c) CV scans of bulk polycrystalline silver exposed to 5 mM 2-CEES in degassed 8.0 M KOH. Black scans represent pre-exposure conditions while the red scans correspond to 5 cycles post-exposure. Experiments conducted at 150 mV/s scan rate between -0.5 and 0.9 V *vs.* Ag/AgCl. SEM images of silver NP-decorated ITO cycled in (d) degassed 8.0 M KOH exposed to 1 mM 2-CEES and in (e) degassed uncontaminated 8.0 M KOH.

An interesting effect is the depletion of β-oxide peak (C_0) resulting in the growth of surface oxide peak (C_1). Unlike DECP, 2-CEES does not cause dissolution and loss of Ag. The SEM image in Fig. 3.10d was taken after potential cycling of the Ag NP-decorated electrode after exposure to 2-CEES. Energy-dispersive X-ray (EDX) spectroscopy data shows that these aggregates consist essentially of Ag and we have no evidence to suggest the presence of any Cl or S on the surface (Fig. 3.11).

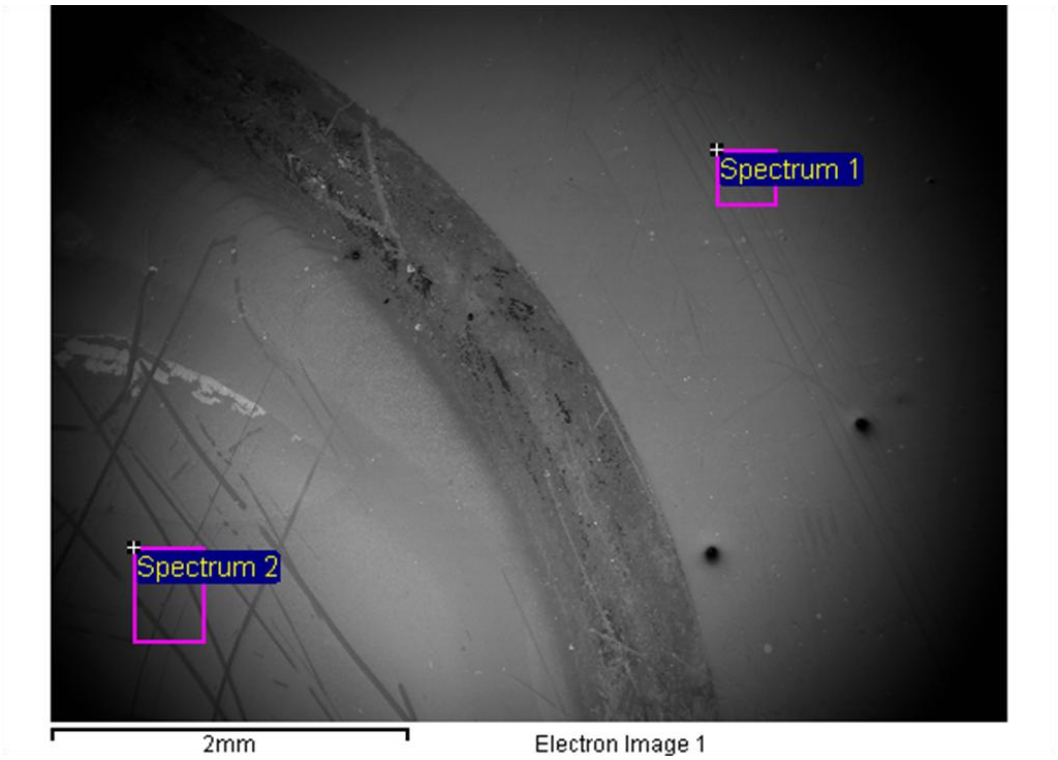

AREA	O (%)	Ag (%)	In (%)
Spectrum 1 (Outside cell)	63.30	7.89	28.81
Spectrum 2 (Inside cell)	64.04	5.52	30.45

Figure 3.11: EDX of silver NP-decorated ITO electrode. Spectrum 2 represents an area exposed to 1 mM 2-CEES cycled in 8.0 M KOH. Spectrum 1 represents an unexposed and uncycled area.

Our observations suggest that 2-CEES reduces β-oxides to metallic Ag which essentially aids in the growth of the Ag NPs into a more bulk-like phase with the associated electrochemical behaviour. This growth is driven by redox cycling resulting essentially in the growth of a bulk Ag phase. In support of this notion, instability observed at high electrolyte concentration (*i.e.*, 8.0 M) with repetitive cycling also lead to a similar evolution of CV in the absence of 2-CEES (Fig. 3.8). Both processes cause the loss of β-oxides and the growth of larger particles,

consistent with an annealing process leading to the loss of a nanostructured surface on which β-oxides form. From our SEM studies, we see a clear topographic difference between aggregates formed in the presence and absence of 2-CEES (Fig. 3.10d and 3.10e, respectively). However, at present we cannot distinguish between aggregates and annealed aggregates and further work is required to solidify the exact mechanism of the 2-CEES effect. It is clear, however, that the chemistry is distinct from that of DECP and that not only do these NP-decorated electrodes prove more sensitive to detection of CWA simulants than bulk, they also allow the types of CWA simulants to be differentiated.

Conclusions. This chapter describes the results of our study of the electrochemical properties of Ag NPs on ITO. We have shown that gas-generated, naked Ag NPs exhibit an electrochemistry that is distinct from that of bulk Ag. For instance, during electrochemical cycling, a significant topographical change is observed on the ITO substrate resulting in NP aggregation. The electrochemical response indicates that Ag NPs possess both analogous and additional redox features compared to bulk, which is the result of their nanoscale size. This in turn, has been exploited for detector capabilities of CWA simulants. Our results indicate that due to the hydrolytic behavior, the addition of cyanide-containing CWA simulants removes Ag from the substrate. At present the working hypothesis is that the cyanide anion generated upon hydrolysis will react with the Ag NPs removing silver off the substrate. In contrast, the sulfur-containing 2-CEES interacts with one of the active oxide phases on the Ag NPs, resulting ultimately in the particle growth and formation of a Ag bulk phase.

Our procedure for NP generation enables the formation of a number of different metal NPs, which in the long term might enable the detection of a range of non-redox active compounds. The next step is to deposit different metals for sensing multiple non-redox compounds with a

single electrode. These initial demonstrations of NP-specific chemistry and the potential for multiplexing, indicate the feasibility for portable multi-sensing devices based on metal NPs.

CHAPTER 4
SUMMARY AND FUTURE RESEARCH

4.1. Summary

The work in this manuscript represents a successful attempt to detect simulants of CWAs *via* electrochemical means. Due to the toxicity and even lethality associated with their exposure, CWA-based research is often restricted requiring several laboratory safety standards for their use; consequently, they are not readily available. An alternative for use of real CWAs in research is the use of structurally similar chemicals referred to as simulants. In this work, DECP and 2-CEES, effective simulants for Tabun nerve agent and blistering sulfur mustard respectively, were utilized. Some of the advantages to work with chemical simulants are that they are commercially available and their toxicity is comparably low; thus, their use only requires common laboratory practices.

An electrochemical logistic problem working with CWAs and their simulants is the fact that they are not redox active. Since electrochemistry studies the electron exchange processes of a system, electrochemistry is not usually associated as a CWA detection technique. Consequently, these compounds are detected by several other methods besides electrochemistry. The approved standard laboratory analytical method for CWA detection and identification is GC-MS. For in-field CWA detection, on the other hand, there is no standard technique. There are, however, several methodologies, such as colourimetric, ion-formation and SAW technologies, which attempt to address this issue. In general, for in-field detection, the applied detection technology should be portable and, ideally, light-weight. This is partially due to the overall detection limitations of in-field detectors and to the common practice of using more than one technology during a single situation for better characterization. The advantage of electrochemistry over other current detection technologies is that it has the potential for

miniaturization and, low requirement for supplies and power, which could lead to ultraportable sensors, in turn reducing fabrication costs.

In order to detect CWA simulants *via* electrochemistry, two approaches were utilized in this research. One of them consisted of a Fc amino acid derivative immobilized on Au surfaces. The Fc amino acid derivative molecule contained, both, a Boc-protected amino group that acted as the reacting site for the simulant and a Fc redox molecule which formal potential is affected by the electronic microenvironment, allowing for non-redox compound detection. This derivative also contained a disulfide bond allowing for chemisorption onto Au, facilitating film formation onto the surface. A few hurdles were encountered with this system, including film formation and Boc-deprotection. The film formation process by self-assembly of thiols (in this case, dialkyl disulfide) onto Au is well known; however, several parameters play a role in the quality of this process leading to variability among films even under the same preparation conditions. The process of potential assisted deposition, or electrodeposition, resulted in reproducible, higher surface coverage and stable films than SAM processes. An additional problem was the method for Boc deprotection. The procedure resulted in a significant loss of signal due to the harsh conditions required for deprotection. Finally, simulant detection using this system was not achieved; however, detection of a compound containing a Cl ligand (*i.e.*, acetyl chloride) produced a potential shifting when compared to the Boc-protected and deprotected states of the film. The results indicate that the Fc amino acid system reacting with simulants might be kinetically hindered.

The deprotection process and, overall, the surface problems encountered with the Fc amino acid derivative, lead to investigate a completely different strategy involving NPs. In general, NPs have shown to be catalytically reactive in several research fields and they have been used to

detect, for example, pesticides. The advantage of our NP synthesis process over the most common solution synthesis, is that our NPs are gas generated requiring no chemical stabilizers (*i.e.*, they are effectively naked). This allows for direct contact between the NPs and the electrode surface, as well as, the analyte under study. The synthesis process also allows for deposition on any substrates, in our case ITO-covered glass plates. Preparation of Ag NPs/ITO working electrodes was relatively quick, easy, and utilization (*i.e.*, free of deprotection) was advantageous. Most importantly these NPs showed redox chemistry which allowed for the indirect detection of CWA simulants. By altering the electrochemical conditions, specifically electrolyte concentration and applied potential range, on the same unfunctionalized Ag NPs on ITO we were able to detect 1 mM quantities of DECP and 2-CEES. DECP, a cyano-containing chemical, is detected *via* silver dissolution resulting in CV signal decrease from an otherwise stable surface-oxide Ag (I) redox signal. On the other hand, 2-CEES is detected by a chemical reaction with β-oxides leading to their depletion. β-oxides are an active oxide species preferentially formed on NPs placing themselves over the surface oxides. Detection is determined during CV scans by the disappearance of the β-oxide peak and the appearance of surface oxides otherwise not observed. Finally, analogue detection electrochemistry for either set of conditions is not observed in bulk polycrystalline Ag.

4.2. Future Research

The next step for the Fc amino acid derivative is to find mild conditions for Boc-deprotection in which signal loss is minimized. This could be researched by a combination of different parameters such as the use of different acids; experimenting with different acid concentrations and exposure times; and the use of a buffer as an electrolyte which would allow to skip the amino deprotonation step after Boc-deprotection. An effect that would be of interest is the use of

different length alkanethiols for backfilling that could offer better film stability. Most importantly is to study the kinetics of the system in order to understand the encountered lack of reactivity with CWA simulants but not with acetyl chloride.

For the Ag NP/ITO system, it would be interesting to further study the mechanism of 2-CEES and its effect on the NPs and the associated annealing of NP aggregates. In general, our NP synthesis procedure allows for the preparation of other metal NPs which could be utilized for a combinatory analysis approach for a variety of non-redox compounds.

Finally, other critical investigations that need to be completed for both systems are detection limits, the possible interferences from common in-field chemicals and, ultimately, testing with real CWAs.

CHAPTER 5
EXPERIMENTAL

5.1. Electrochemical Experiments

All electrochemical experiments were performed on a CHI660B electrochemical workstation (CH Instruments Inc.). Experiments were performed inside a copper mesh Faraday cage designed to isolate the electrochemical system by blocking external electrical fields. All CV and LSV experiments were started at the open circuit potential of the specific run. This potential value was obtained by utilizing the command, of the same name, found on the Control menu bar. The open circuit potential is the potential of the working electrode relatively to the reference electrode at which there is no current or potential transfer at the working electrode. This resting potential effectively allows the system to start at a non-shocking potential, which could otherwise damage the film at the working surface.

In most cases, the electrochemical system was utilized in a 3-electrode set up. All potentials quoted refer to Ag/AgCl reference electrode (3.0 M NaCl, Bioanalytical Systems Inc.). A Pt wire (0.5 mm diameter, 99.95%, Alfa Aesar) served as the auxiliary electrode. The reference electrode was connected to the system via a 1.0 mM KNO_3 – 5% agar salt bridge. In rare experiments, the system only required 2 electrodes. In these cases, the reference electrode was not present.

For most electrochemical experiments, the electrochemical cell consisted of 20 mL borosilicate glass vials. However, when Ag NP/ITO modified electrodes were used, a 5 mL homebuilt Teflon® cell was utilized. This cell also had a Teflon® cover allowing positioning the electrodes at the same space intervals, minimizing variation from experiment to experiment.

Prior to experimentation, supporting electrolyte was de-aerated with N_2 for at least 15 min and an inert blanket of the same gas was maintained during the experiments. All aqueous supporting

electrolyte solutions were prepared with MilliQ (Millipore™) water. All ethanol-based supporting electrolyte solutions were distilled to remove impurities.

5.2. Electrode Preparation

5.2.1. Gold Microelectrodes Preparation and Characterization

Au MEs were prepared by heat-melting a borosilicate glass capillary onto a 50 µm Au wire. For electrical contact, a conductive wire was soldered to the Au wire with Sn metal. In order to add robustness, shrinking plastic tube was melted over the connection of the borosilicate glass and the conductive wire. Once constructed, MEs were manually polished with sand paper of different grades (*i.e.*, from rough to fine grade in that sequence), followed by polishing with a 48000 Micropipette Beveler (World Precision Instruments Inc.) on wet 3 µm and 0.3 µm alumina films sequentially in that order. Their connectivity was tested in aqueous 0.5 M H_2SO_4 while observing the typical Au redox CV scan and peak potentials. Finally, MEs were characterized by Cu UPD.

Cu UPD allowed determining the surface roughness of Au MEs, based on their experimental calculated area. For Cu UPD, in a 3-electrode system, a pre-condition step was performed in a solution of 2.0 mM $Cu(ClO_4)_2 \cdot 6H_2O$ in 1.0 M $HClO_4$ electrolyte, followed by LSV technique. This pre-conditioning step consisted of applying a 500 mV voltage for 30 s allowing for the deposition of a monolayer of Cu atoms on the surface of the Au electrode. Then, LSV was performed to the modified ME to strip off the Cu atoms physisorbed to the surface. To achieve this step, a potential window from 50 to 750 mV at 100 mV/s scan rate was applied. The integration of the anodic peak produced by the stripping LSV process resulted in the charge value present on the Au electrode. The integrated charge, in units of Coulombs, allowed

calculating mathematically the experimental real area and the roughness factor. All working Au MEs had a roughness factor between 1.1 and 1.4.

An example is described to illustrate this process. An experimental LSV peak integration resulted in an area of 6.413×10^{-9} C. This charge corresponds to the reduction of the Cu monolayer on the Au surface. Cu reduction involves a 2-electron process (*i.e.*, $Cu^{2+} \rightarrow Cu^{0}$). Hence, this area must be divided by a factor of 2. To obtain the number of moles of Cu, this charge value is divided by Faraday's constant: 96485.3 C/mol. To obtain the number of atoms of Cu, the value is further divided by Avogadro's number: 6.02×10^{23} atoms/mol. In this case, the integrated peak area resulted in 2.00E+10 Cu atoms. From literature,[115] the number of Cu atoms in a monolayer formed onto Au surface (*i.e.*, onto Au atoms) is approximately 2 Cu atoms per 3 Au atoms. Also from literature,[41] the number of Au atoms on an ideal atomically flat surface (*i.e.*, a 111 Miller index) is 1.5×10^{15} atoms/cm^2. Multiplying these two literature values, the ideal number of Cu atoms per area in cm^2 units, can be calculated as 1.0×10^{15} Cu atoms/cm^2. Dividing the experimental number of Cu atoms by the ideal number, the real area of the Au ME can be obtained. In this particular case, an area of 2.0×10^{-5} cm^2. Finally, to determine the roughness factor, the experimental area is divided by the ideal area of a 50 μm round wire (*i.e.*, utilizing the formula $A = \pi * r^2$), in this case resulting in 1.02.

5.2.2. Silver Nanoparticle-Decorated Indium-Tin Oxide Electrode

Gas-generated Ag NPs were deposited onto ITO substrates. NP density on the ITO surface was controlled by deposition time. ITO substrates (8–12 ohms, SPI Supplies) were used as received. For our experiments, Ag was deposited onto ITO for 7.5 min resulting in a mass addition of 1.5 ± 0.5 μg. The Ag NP/ITO electrodes were stored at room temperature under atmospheric conditions until use (usually within days).

5.2.3. Silver Electrode

Polycrystalline Ag working electrodes were prepared to represent bulk Ag. These electrodes were prepared from 1.0 mm diameter Ag wire (99.999 %, Alfa Aesar) which was sealed in borosilicate glass capillaries (preparation was similar to Au ME). The working area, of *ca*. 0.78 mm^2, was polished sequentially with 0.3 and 0.05 μm alumina slurry for 10 min each prior to use. Electrochemical experiments with polycrystalline electrodes were performed in glass vials.

5.3. Ferrocene Amino Acid Derivative Film Formation

The Fc amino acid derivate compound utilized was $[(BocHN)Fc(CO)CSA]_2$. Initially, films were prepared by passive-solution deposition.[56] Fully characterized Au MEs were electrochemically first treated to remove unwanted bound material on the surface by applying a large potential window from -1.9 to 2.0 V in 0.5 M H_2SO_4 using a 2-electrode system *vs.* Pt wire for 15 cycles. MEs were then moved to a 3-electrode system in which the Ag/AgCl reference electrode connectivity was assisted with a salt-bridge. In this set-up, a smaller potential window from 0.2 to 1.6 V was applied for 15 cycles. Finally, the sides of the MEs were immediately dried with a Kimwipe tissue before being immersed in a 1 mM ethanolic solution of the Fc amino acid derivative. After a 5-day incubation period, ME's were rinsed with copious amounts of distilled ethanol followed by MilliQ water. To further remove any physisorbed molecules, the MEs were sonicated for 2–10 seconds in ethanol followed by backfilling with 1 mM ethanolic solution of butanethiol for 5 min.

A second method to form films on Au surfaces consisted of potential-assisted deposition.[74,116] Before performing electrodeposition, MEs were pre-treated in two stages by cycling in 0.5 M H_2SO_4 using a 2-electrode system *vs.* Pt wire. The first stage purpose was to oxidize the surface by applying a potential window ranging from -0.4 to 1.0 V for 21 segments at 10 V/s. A subsequent pre-treatment cycling between -0.6 to -2.3 V for 20 segments at 10 V/s helped with desorption of O atoms and the adsorption of H atoms onto the Au surface. The purpose of the last step was to avoid the possibility for sulfonate formation (*i.e.*, $R–S(=O)_2O–Au$) between the Fc derivative sulfur end and the oxidized Au surface; thus, ensuring formation for a stronger chemisorbed RS–Au bond.[116]

A 1 mM solution of $[(BocHN)Fc(CO)CSA]_2$ in distilled ethanol was prepared for electrodeposition. This ethanolic solution was de-aired in N_2 for at least 15 min prior to use and a blanket of the same inert gas was maintained during the of the experiment Treated ME's were immersed into this solution and a potential of -1.8 V *vs.* Ag wire was applied for 30 min. Once electrodeposited onto Au, films were sonicated in distilled ethanol for 30–60 sec in order to remove Fc derivative molecules physisorbed and/or weakly absorbed onto the surface of the electrode; effectively removing multilayers formed during the process. Films were further diluted with an ethanolic solution of 1 mM butanethiol in order to cover any exposed Au surface; effectively removing Au for possible redox process. Film formation, was confirmed by anodic peak integration of the CV produced by the film in 2.0 M $NaClO_4$ electrolyte in a 3-electrode system assisted with a salt-bridge at a scan rate of 100 mV/s.

5.3.1. Boc Deprotection

Boc-protecting group removal was achieved by incubating film-modified Au MEs for 1 min in a solution of 10% TFA in DCM, followed by 10 sec in a solution of 10 % Et_3N in DCM solution. Exposure to CWA simulants followed immediately after deprotection.

5.4. Silver Nanoparticle Synthesis

Ag NPs were made with a gas-phase generator and immediately deposited on ITO substrates.[101] Briefly, an applied potential between an anode cap and the Ag metal disc target generates a discharge, which creates ions from the Ar gas flushing the system. Energetic Ar^+ then bombard the negatively biased bulk metal Ag target liberating metal atoms to the gas phase. Metal atoms leave the sputtering region mobilized by Ar flow and enter the aggregation zone. There, the relative high pressure facilitates frequent collisions of the Ag metal atoms and NPs form. Next, the Ag NPs enter the low-pressured deposition chamber and are collected onto ITO substrates. NP density on the ITO surface is controlled by deposition time.

5.5. Surface Characterization

There were several techniques utilized to characterized surfaces: SEM images were obtained using a Leo 1540XB SEM CrossBeam Workstation, which was equipped with EDX for composition analysis. A Schottky field emission tip (ZrO/W-cathode) was used as a beam generator. Images were obtained using the secondary electron mode with no tilt. AFM images were obtained by dynamic force AFM (XE–100 PSIA) using a silicon cantilever. The cantilever had a spring constant of *ca.* 40 N/m. The cantilever was 125 μm long, 30 μm wide, 3.7 μm thick and its tip apex of 10–20 nm radius. This tip was used to probe the morphology of the sample surface. By definition, in a non–contact dynamic mode, a constant damped amplitude between

the oscillating cantiliver tip and the sample surface allowed for surface morphology imaging. Collected AFM images were analyzed using XEI software (PSIA Inc.).

LIST OF REFERENCES

1. P. A. D'Agostino and C. L. Chenier, Technical Report March 2006, DRDC Suffield TR 2006–022.

2. P. A. D'Agostino, in *Handbook of Analytical Separations*, ed. M. J. Bogusz, Elsevier, 1st edn., 2008, vol. 6, ch. 25, pp. 839–872.

3. L. Szinicz, *Toxicology*, 2005, **214**, 167–181.

4. L. D. Prockop, *J. Neurol. Sci.*, 2006, **249**, 50–54.

5. J. Newmark, *Neurology*, 2004, **62**, 1590–1596.

6. F. Schmaltz, *J. Hist. Neurosci.*, 2006, **15**, 186–209.

7. R. E. Langford, in *Introduction to Weapons of Mass Destruction*, Wiley-Interscience, 2004, ch. 12, pp. 218.

8. J. B. Tucker, in *War of Nerves*, Anchor Books, 2006, ch. 9, pp. 181-182.

9. P. M. Lundy, M. G. Hamilton, I. Hill, J. Conley, T. W. Sawyer and D. C. Caneva, *Mil. Med.*, 2004, **169**, 856–862.

10. S. Royo, R. Martínez-Máñez, F. Sancenón, A. M Costero, M. Parra and S. Gil, *Chem. Commun.*, 2007, **46**, 4839–4847.

11. A. B. Kanu, P. E. Haigh and H. H., *Anal. Chim. Acta*, 2005, **553**, 148–159.

12. Committee on Toxicology, National Research Council. *Review of Acute Human-Toxicity Estimates for Selected Chemical-Warfare Agents*; National Research Council, National Academy Press: Washington, DC, 1997.

13. H. K. Khordagui, *Sci. Global Sec.*, 1997, **6**, 239–263.

14. T. Wada, E. Nagasawa and S. Hanaoka, *Appl. Organomet. Chem.*, 2006, **20**, 573-579.

15. R. Haas, *Environ. Sci. Pollut. R.*, 1998, **5**, 2-3.

16. A. E. F. Nassar, S. V. Lucas and L. D. Hoffland, *Anal. Chem.*, 1999, **71**, 1285-1292.

17. G. L. Kimm, G. L. Hook and P. A. Smith, *J. Chromatogr. A*, 2002, **971**, 185-191.

18. J. A. Diaz, P. Daley, R. Miles, H. Rohrs and D. Polla, *Trends Anal. Chem.*, 2004, **23**, 314–321.

19. From the Organisation for the Prohibition of Chemical Weapons internet website http://www.opcw.org/about-opcw/ [Retrieved on 6 July 2009].

20. T. L. Sheehan, *Am. Lab.*, 2002, **34**, 40-43.

21. E. W. J. Hooijschuur, C. E. Kientz and U. A. T. Brinkman, J. *Chromatogr. A*, 2002, **982**, 177-200.

22. R. M. Black and B. Muir, *J. Chromatogr. A*, 2003, **1000**, 253-281.

23. P. A. Smith, C. R. Jackson-LePage, D. Koch, H. D. M. Wyatt, G. L. Hook, G. Betsinger, R. P. Erickson and B. A. Eckenrode, *Trac-Trend. Anal. Chem.*, 2004, **23**, 296-306.

24. A. Keil, N. Talaty, C. Janfelt, R. J. Noll, L. Gao, Z. Ouyang and R. G. Cooks, *Anal. Chem.*, 2007, **79**, 7734-7739.

25. Z. Ouyang, G. Wu, Y. Song, H. Li, W. R. Plass and R. G. Cooks, *Anal. Chem.*, 2004, **76**, 4595-4605.

26. D. E. P. Turl and D. R. W. Wood, *Analyst*, 2008, **133**, 558-562.

27. Y. Sun and K. Y. Ong, in *Detection Technologies for Chemical Warfare Agents and Toxic Vapors*, CRC Press, Florida, 1st edn., 2004, ch. 10, pp. 198-206.

28. Committee on R&D Needs for Improving Civilian Medical Response to Chemical and Biological Terrorism Incidents, Institute of Medicine. *Chemical and Biological Terrorism*; National Research Council, National Academy Press: Washington, DC, 1999.

29. Y. Seto, M. Kanamori-Kataoka, K. Tsuge, I. Ohsawa, K. Matsushita, H. Sekiguchi, T. Itoi, K. Iura, Y. Sano and S. Yamashiro, *Sensor. Actuator. B*, 2005, **108**, 193-197.

30. Science Encyclopedia Vol. 3, Ion and Ionization – Ionization Methods, p. 3678, http://science.jrank.org/pages/3678/Ion-Ionization-Ionization-methods.html [Retrieved on 18 July 2009].

31. H. H. Hill Jr. and S. J. Martin, *Pure Appl. Chem.*, 2002, **74**, 2281-2291.

32. R. Weigel, D. P. Morgan, J. M. Owens, A. Ballato, K. M. Lakin, K.-Y. Hashimoto and C. C. W. Ruppel, *IEEE Microw. Theory*, 2002, **50**, 738-749.

33. S. Kendler, A. Zaltsman and G. Frishman, *Instrum. Sci. Technol.*, 2003, **31**, 357-375.

34. M. W. P. Petryk, *Appl. Spectrosc. Rev.*, 2007, **42**, 287-343.

35. S. K. Ross, G. McDonald and S. Marchant, *Analyst*, 2008, **133**, 602-607.

36. Y. Wei, Y. Li, Y. Qu, F. Xiao, G. Shi and L. Jin, *Anal. Chim. Acta*, 2009, **643**, 13-18.

37. M. A. K. Khan, K. Kerman, M. Petryk and H.-B. Kraatz, *Anal. Chem.*, 2008, **80**, 2574-2582.

38. A. J. Marenco, D. B. Pedersen, S. Wang, M. W. P. Petryk and H.-B. Kraatz, *Analyst*, 2009, **134**, 2021-2027.

39. U. Guth, W. Vonau and J. Zosel, *Meas. Sci. Technol.*, 2009, **20**, 1-14.

40. Y. Wang, H. Xu, J. Zhang and G. Li, *Sensors*, 2008, **8**, 2043-2081.

41. A. J. Bard and L. R. Faulkner, in *Electrochemical Methods: Fundamentals and Applications*, 2nd edn., Wiley, New York, 2000.

42. J. O'M. Bockris and A. K. N. Reddy, in *Modern Electrochemistry Vol. 2*, Plenum Press, New York, 1970, ch. 7, pp. 623-625.

43. A. Kisza, *Electrochim. Acta.*, 2006, **51**, 2315-2321.

44. I. Bediako-Amoa, T. C. Sutherland, C.-Z. Li, R. Silerova and H.-B. Kraatz, *J. Phys. Chem. B*, 2004, **108**, 704-714.

45. Pine Instrument Company. *Educator's Reference Guide for Electrochemistry*; Revision 003, Pennsylvania, 2000, pp. 2.

46. S. P. Kounaves, in *Handbook of Instrumental Techniques for Analytical Chemistry*; ed. F. A. Settle, Prentice Hall, 1997, section 4, ch. 37, pp. 711-728.

47. Princeton Applied Research. *A Review of Techniques for Electrochemical Analysis*, Application Note E-4, pp. 1-12.

48. D. H. Evans, *Accounts Chem. Res.*, 1977, **10**, 313-319.

49. G. Leftheriotis, S. Papaefthimiou and P. Yianoulis, *Solid State Ionics*, 2007, **178**, 259-263.

50. V. Gau, S.-C. Ma, H. Wang, J. Tsukuda, J. Kibler and D. A. Haake, *Methods*, 2005,**37**, 73-83.

51. P. Laszlo and R. Hoffmann, *Angew. Chem. Int. Ed.*, 2000, **39**, 123-124.

52. M. F. R. Fouda, M. M. Abd-Elzaher, R. A. Abdelsamaia and A. A. Labib, *Appl. Organometal. Chem.*, 2007, **21**, 613-625.

53. T. M.-H. Lee and I-M. Hsing, *Anal. Chim. Acta*, 2006, **556**, 26-37.

54. K. Plumb and H.-B. Kraatz, *Bioconjugate Chem.*, 2003, **14**, 601-606.

55. L. Barisic, M. Cakic, K. A. Mahmoud, Y.-N. Liu, H.-B. Kraatz, H. Pritzkow, S. I. Kirin, N. Metzler-Nolte and V. Rapic, *Chem.-Eur. J.*, 2006, **12**, 4965-4980.

56. M. A. K. Khan, Y.-T. Long, G. Schatte and H.-B. Kraatz, *Anal. Chem.*, 2007, **79**, 2877-2884.

57. M. A. K. Khan, D. S. Thomas and H.-B. Kraatz, *Inorg. Chim Acta.*, 2006, **359**, 3339-3344.

58. R. J. Forster and L. R. Faulkner, *J. Am. Chem. Soc.*, 1994, **116**, 5444-5452.

59. R. Heinz and J. P. Rabe, *Langmuir*, 1995, **11**, 506-511.

60. C. Schönenberger, J. A. M. Sondag-Huethorst, J. Jorritsma and L. G. J. Fokkink, *Langmuir*, 1994, **10**, 611-614.

61. J. C. Love, L. A. Estroff, J. K. Kriebel, R. G. Nuzzo and G. M. Whitesides, *Chem. Rev.*, 2005, **105**, 1103-1169.

62. A. Badia, R. B. Lennox and L. Reven, *Acc. Chem .Res.*, 2000, **33**, 475-481.

63. M. D. Porter, T. B. Bright, D. L. Allara and C. E. D. Chidsey, *J. Am. Chem. Soc.*, 1987, **109**, 3559-3568.

64. G. Nelles, H. Schönherr, G. J. Vancso and H.-J. Butt, *Appl. Phys. A*, 1998, **A66**, S1261-S1266.

65. C. Vericat, M. E. Vela, G. A. Benitez, J. A. Martin-Gago, X. Torrelles and R. C. Salvarezza, *J. Phys.- Condens. Mat.*, 2006, 18, R867-R900.

66. H.-T. Rong, S. Frey, Y.-J. Yang, M. Zharnikov, M. Buck, M. Wühn, C. Wöll and G. Helmchen, *Langmuir*, 2001, **17**, 1582-1593.

67. J. M. Harrowfield, G. A. Koutsantonis, H.-B. Kraatz, G. L. Nealon, G. A. Orlowski, B. W. Skelton and A. H. White, *Eur. J. Inorg. Chem.*, 2007, 263-278.

68. C. Jung, O. Dannenberger, Y. Xu, M. Buck and M. Grunze, *Langmuir*, 1998, **14**, 1103-1107.

69. L. Y. S. Lee and R. B. Lennox, *Phys. Chem. Chem. Phys.*, 2007, **9**, 1013-1020.

70. F. Ma and R. B. Lennox, *Langmuir*, 2000, **16**, 6188-6190.

71. M. Sheffer, V. Vivier and D. Mandler, *Electrochem. Commun.*, 2007, **9**, 2827-2832.

72. S. W. Han, H. Seo, Y. K. Chung and K. Kim, *Langmuir*, 2000, **16**, 9493-9500.

73. T. Wink, S. J. van Zuilen, A. Bult and W. P. van Bennekom, *Analyst*, 1997, **122**, 43R-50R.

74. G. A. Orlowski, S. Chowdhury, Y.-T. Long, T. C. Sutherland and H.-B. Kraatz, *Chem. Commun.*, 2005, 1330-1332.

75. K. Yoshizawa-Kumagaye, Y. Nishiuchi, H. Nishio and T. Kimura, *J. Peptide Sci.*, 2005, **11**, 512-515.

76. J. Wang, *Analyst*, 2005, **130**, 421-426.

77. G. Oberdörster, E. Oberdörster and J. Oberdörster, *Environ. Health Persp.*, 2005, **113**, 823-839.

78. D. M. Adams, L. Brus, C. E. D. Chidsey, S. Creager, C. Creutz, C. R. Kagan, P. V. Kamat, M. Lieberman, S. Lindsay, R. A. Marcus, R. M. Metzger, M. E. Michel-Beyerle, J. R. Miller, M. D. Newton, D. R. Rolison, O. Sankey, K. S. Schanze, J. Yardley and X. Zhu, *J. Phys. Chem. B*, 2003, **107**, 6668-6697.

79. Y. B. Pithawalla, M. S. El-Shall, S. C. Deevi, V. Ström and K. V. Rao, *J. Phys. Chem. B,* 2001, **105**, 2085-2090.

80. C. M. Welch and R. G. Compton, *Anal. Bioannal. Chem.*, 2006, **384**, 601-619.

81. G. J. Hutchings and M. Haruta, *Appl. Catal. A: Gen.*, 2005, **291**, 2-5.

82. A. P. Weber, M. Seipenbusch and G. Kasper, *J. Nanopart. Res.*, 2003, **5**, 293-298.

83. J. Kreuter, *Int. J. Pharm.*, 2007, **331**, 1-10.

84. E. C. Walter, F. Favier and R. M. Penner, *Anal. Chem.*, 2002, **74**, 1546-1553.

85. S. E. Cross, B. Innes, M. S. Roberts, T. Tsuzuki, T. A. Robertson and P. McCormick, *Skin Pharmacol. Physiol*, 2007, **20**, 148-154.

86. G. Schmid, Ed. Nanoparticles – From Theory to Application 3rd edition 2005Wiley-Vch.

87. R. L. Johnston, *Phil. Trans. R. Soc. Lond. A*, 1998, **356**, 211-230.

88. A. R. West, Ed. Basic Solid State Chemistry 2nd edition 1999 John Wiley & Sons.

89. A. P. Alivisatos, *Endeavour*, 1997, **21**, 56-60.

90. J. P. Wilcoxon and B. L. Abrams, *Chem. Soc. Rev.*, 2006, **35**, 1162-1194.

91. C. P. Poole, Jr. and F. J. Owens, Introduction to Nanotechnology, 2003, John Wiley & Sons.

92. R. J. Gilliam, D. W. Kirk and S. J. Thorpe, *Electrochem. Comm.*, 2007, **9**, 875-878.

93. D. R. Kauffman and A. Star, *Angew. Chem. Int. Ed.*, 2008, **47**, 2-23.

94. C. B. Murray, C. R. Kagan and M. G. Bawandi, *Annu. Rev. Mater. Sci.*, 2000, **30**, 545-610.

95. L. C. Nagle, A. J. Ahern and L. D. Burke, *J. Solid State Electrochem.*, 2002, **6**, 320-330.

96. J. Meier, J. Schiøtz, P. Liu, J. K. Nørskov and U. Stimming, *Chem. Phys. Lett.*, 2004, **390**, 440-444.

97. X. Dai, G. G. Wildgoose, C. Salter, A. Crossley and R. G. Compton, *Anal. Chem.*, 2006, **78**, 6102-6108.

98. R. E. Dávila-Martínez, L. F. Cueto and E. M. Sánchez, *Surf. Sci.*, 2006, **600**, 3427-3435.

99. G. Sandmann, H. Dietz and W. Plieth, *J. Electroanal. Chem.*, 2000, **491**, 78-86.

100. G.S. Hsiao, M. G. Anderson, S. Gorer, D. Harris and R. M. Penner, *J. Am. Chem. Soc.*, 1997, **119**, 1439-1448.

101. D. B. Pedersen and S. Wang, *J. Phys. Chem. C.*, 2007, **111**, 1261-1267.

102. D. B. Pedersen and S. Wang, *J. Phys. Chem. C.*, 2009, **113**, 4797-4803.

103. K. A. Mahmoud, S. Hrapovic and J. H. T. Luong, *ACS Nano*, 2008, **2**, 1051-1057.

104. T. U. Hur and W. S. Chung, *J. Electrochem. Soc.*, 2005, **152**, A996-A1000.

105. J. Pan, Y. Sun, Z. Wang, P. Wan, X. Liu and M. Fan, *J. Mater. Chem.*, 2007, **17**, 4820-4825.

106. S. J. Xia and V. I. Birss, *J. Electroanal. Chem.*, 2001, **500**, 562-573.

107. S. J. Xia and V. I. Birss, *Electrochim. Acta*, 2000, **45**, 3659-3673.

108. J. Szymanska, M. J. Palys and B. Van den Bossche, *Anal. Chem.*, 2004, **76**, 5937-5944.

109. R. D. Vengrenovich, Y. V. Gudyma and S. V. Yarema, *Semiconductors+*, 2001, **35**, 1378-1382.

110. P. L. Redmond, A. J. Hallock and L. E. Brus, *Nano Lett.*, 2005, **5**, 131-135.

111. C. W. Griffin, in *Inorganic Quantitative Analysis*, Read Books, 2007, Ch. 16, p. 284-285.

112. N. B. Munro, S. S. Talmage, G. D. Griffin, L. C. Waters, A. P. Watson, J. F. King and V. Hauschild, *Environ. Health Persp.*, 1999, **107**, 933-974.

113. A. Michalkova, M. Ilchenko, L. Gorb, J. Leszczynski, *J. Phys. Chem. B*, 2004, **108**, 5294-5303.

114. V. Štengl, S. Bakardjieva, M. Maříková, J. Šubrt, F. Opluštil, M. Olšanská, *Cent. Eur. J. Chem.*, 2004, **2**, 16-33.

115. V. Sudha and M. V. Sangaranarayanan, *J. Chem. Sci.*, 2005, **117**, 207-218.

116. G. A. Orlowski, S. Chowdhury and H.-B. Kraatz, *Langmuir*, 2007, **23**, 12765-12770.